

# **Designing and Commissioning of a Prototype High Energy Resolution Fluorescence Detection System at the Canadian Light Source**

by

Evan Thomas

A Thesis

presented to

The University of Guelph

In partial fulfilment of requirements  
for the degree of

Masters

in

Physics

Guelph, Ontario, Canada

© Evan Thomas, January, 2021

# ABSTRACT

## DESIGNING AND COMMISSIONING OF A PROTOTYPE HIGH ENERGY RESOLUTION FLUORESCENCE DETECTION SYSTEM AT THE CANADIAN LIGHT SOURCE

Evan Hospur Thomas  
University of Guelph, 2021

Advisor:  
Dr. De-Tong Jiang

This thesis can be viewed as a feasibility study into running a High Energy Resolution Fluorescence Detection system for x-ray absorption spectroscopy at the Hard X-ray MicroAnalysis beamline at the Canadian Light Source. This study was carried out through the construction of an x-ray photon energy analyzer system based around a single Johann crystal on a Rowland circle with a half meter diameter. Using this system high resolution scans of cinnabar ( $\text{HgS-}\alpha$ ) and metacinnabar ( $\text{HgS-}\beta$ ) were collected and compared to conventional fluorescence results. A dramatic increase in spectral sharpness was observed showing the validity and capability of this technique. The results attained are comparable to results acquired at other synchrotron facilities using a variety of x-ray sources and beamline optics. Further testing and refinement at HXMA is expected to progress this technique to a user operable state. Ideally this work is just the first steps in making High Energy Resolution Fluorescence detection available in Canada.

## DEDICATION

To my parents, I could not be who I am today without your guidance, encouragement and love. While I can never truly repay you, I will try to do well by all that you continue to do for me.

To Bailey, your never-ending support, constant care and innate ability to keep me sane makes everyday a blessing. Thank you.

## ACKNOWLEDGEMENTS

I would like to thank the Canadian Light Source for their project funding and support throughout this study. I would like to thank the HXMA beamline and its associated beamteam especially Dr. Ning Chen and Dr. Weifeng Chen. Ning taught me much of what I know about being a scientist and showed the benefit of staying positive. Weifeng facilitated this project coming together, through purchasing commercial parts and components as well as ensuring their safe shipping from the CLS to the University of Guelph.

I would also be remiss not to thank my lab mate Cameron McGuire for his help and support on and off the beamline. Without his help at the beamline I may have never slept, and the results of this thesis surely wouldn't be as refined. In addition, I would like to thank Dr. Zachary Arthur for his support while at CLS.

The University of Guelph Physics department staff also provided much needed support, especially Rachel Baker who facilitated materials shipping, part acquisition and travel arrangements. A large thank you also goes out to the Physics Machine Shop, especially Ian Moore and Steve Wilson for their design expertise and for manufacturing many components essential to the experimental system.

Finally, I would like to thank my advisor Dr. De-Tong Jiang who has taught me practically all I know about being an experimentalist. Only through his immense dedication, countless hours and mentorship was this project possible. Thank you for sharing your wealth of knowledge and pushing me to seek a deep understanding of all that is associated with beamline science.

# TABLE OF CONTENTS

Abstract.....	ii
Dedication .....	iii
Acknowledgements .....	iv
Table of Contents.....	v
List of Figures.....	vii
List of Abbreviations.....	ix
List of Appendices.....	x
1 Introduction .....	1
1.1 Project History and Motivation.....	1
1.2 High Resolution Fluorescence Detection .....	3
1.3 Overview of Work.....	5
2 Theory and Background.....	7
2.1 X-ray Absorption Fine Structure .....	7
2.2 XAFS Instrumentation Basics.....	10
2.2.1 Transmission Mode .....	12
2.2.2 Fluorescence Mode .....	13
2.3 Improving Fluorescence Resolution .....	16
2.3.1 Resonant X-ray Emission Spectroscopy Methods and Mapping .....	19
2.4 High Energy Resolution Fluorescence Detection .....	23
2.4.1 Bragg Reflective Fluorescence Detection.....	26

2.4.2	Energy Mapping Using a Johann Bragg System .....	31
3	Instrumentation and Construction .....	33
3.1	Canadian Light Source: HXMA Beamline .....	33
3.2	Design and Construction .....	35
3.2.1	Spherically Bent Silicon Crystal Analyzer .....	36
3.2.2	Energy Resolving Detector .....	38
3.2.3	Motor Controls and Moving on the Rowland Circle.....	39
3.3	Sample Selection and Preparation.....	44
4	Experimentation and Data Analysis .....	48
4.1	Intended Scanning Routine .....	48
4.2	Comparison to Published Results .....	56
4.3	Intended Procedures for RIXS Mapping.....	63
4.4	Testing in Vertical Rowland Circle Configuration .....	66
5	Further Developments and Conclusions .....	71
5.1	Area detection and ray tracing .....	71
5.2	Moving Vertical using a Multi-crystal analyzer system .....	72
5.3	Low Energy Extension .....	74
5.4	Concluding Remarks.....	75
	Bibliography .....	78
	Appendix A: Motion Controls for the HERFD System .....	81
	Appendix B: Energy Range of Various Silicon Crystals.....	83

## LIST OF FIGURES

<b>Figure 2.1:</b> A normalized absorption spectra of cinnabar mercury sulfide illustrating the boundary between XANES and EXAFS .....	9
<b>Figure 2.2:</b> A schematic of a typical set-up for a transmission mode measurement, using three ionization chambers.....	12
<b>Figure 2.3:</b> Fluorescence photon production through an x-ray absorption that creates a core-hole via a K-edge excitation .....	14
<b>Figure 2.4:</b> A schematic of a fluorescence mode measurement, using three ionization chambers to measure incident intensity and the absorption of a reference sample. In addition, a fourth detector is used to measure fluorescence intensity .....	16
<b>Figure 2.5:</b> The fluorescence process of an $L_3$ excitation resulting in a 2p hole that will be filled by a 3d electron .....	18
<b>Figure 2.6:</b> Schematics of the same RIXS map plotted using the two different axis conventions .....	21
<b>Figure 2.7:</b> A schematic view of a portions of a fluorescence band that is integrated in a conventional fluorescence experiment and a HERFD experiment. ....	24
<b>Figure 2.8:</b> A RIXS map displaying the portion of fluorescence that is integrated in a conventional fluorescence experiment and a HERFD experiment in 2-d energy space.	25
<b>Figure 2.9:</b> An illustrative visualization of Johann geometry showing the larger bending radius of the crystal analyzer and beam/fluorescence path.....	29
<b>Figure 2.10:</b> The movements required for an adjustment to a higher analyzed energy are shown by the yellow arrows. Resulting in a decrease in Bragg angle and thus an increase in the allowed reflected energies .....	32
<b>Figure 3.1:</b> A schematic diagram showing the scale and arrangement of the sample, crystal analyzer and detector, respectively, on the Rowland circle .....	36
<b>Figure 3.2:</b> A photo of the Si(1,1,1) strip bent crystal analyzer and the associated rotational axis are depicted . ....	37
<b>Figure 3.3:</b> A schematic diagram of the crystal mount and a photo of the mounted analyzer crystal .....	38
<b>Figure 3.4:</b> A schematic diagram and picture of the analyzer stack used for this experiment. Labeled in the schematic are the control stages used for positioning and scanning.....	41

<b>Figure 3.5:</b> A schematic diagram and picture of the detector stack used for this experiment. Labeled in the schematic are the control stages used for positioning and scanning.....	42
<b>Figure 3.6:</b> The experimental HERFD arrangement viewed from downstream from the sample point.....	43
<b>Figure 3.7:</b> A schematic diagram and image of the prepared sample mounted on a sample slide and secured using Kapton® tape. ....	46
<b>Figure 3.8:</b> Diagrams of the sample structures investigated; cinnabar and metacinnabar .....	47
<b>Figure 4.1:</b> A schematic diagram of the system used for calibration and conventional scans composed of ionization chambers and a Lytle chamber. In addition, the HERFD system is shown positioned downstream from the second ionization chamber.....	49
<b>Figure 4.2:</b> The spectra from conventional fluorescence detection for cinnabar (HgS- $\alpha$ ) and metacinnabar (HgS- $\beta$ ) .....	51
<b>Figure 4.3:</b> The resulting spectra from the conventional fluorescence detection, the misaligned HERFD arrangement and the HERFD arrangement after motor scans. ....	53
<b>Figure 4.4:</b> A schematic RIXS map showing the cause of the apparent edge shift seen when varying the analyzed energy .....	55
<b>Figure 4.5:</b> The final results of the HERFD data collection working with both cinnabar (HgS- $\alpha$ ) and metacinnabar (HgS- $\beta$ ) plotted with the conventional results.....	57
<b>Figure 4.6:</b> Spectra from the mercury LIII edge produced at ESRF on beamline BM16 showing conventional and HERFD results for cinnabar (HgS- $\alpha$ ) and metacinnabar (HgS- $\beta$ ) Source: Proux et. al. 2017, figure 3 (p. 13). [22] Reprinted with permission of John Wiley & Sons. Inc. ....	59
<b>Figure 4.7:</b> The spectra collected at APS for cinnabar (HgS- $\alpha$ ) collected using both conventional fluorescence detection and HERFD. ....	62
<b>Figure 4.8:</b> A schematic diagram of the movements undergone to adjust to a higher analyzed energy.....	65
<b>Figure 4.9:</b> The experimental set-up used for vertical Rowland circle testing.....	68
<b>Figure 4.10:</b> The spectra of cinnabar (HgS- $\alpha$ ) collected using a vertical Rowland circle geometry plotted to show contrast with the conventional HERFD result. ....	69

## LIST OF ABBREVIATIONS

<b>APS:</b>	The Advanced Photon Source
<b>BM:</b>	Bending Magnet
<b>CLS:</b>	The Canadian Light Source
<b>ESRF:</b>	European Synchrotron Radiation Facility
<b>EXAFS:</b>	Extended X-ray Absorption Fine Structure
<b>FDMNES:</b>	Finite Difference Method Near Edge Structure
<b>HERFD:</b>	High Energy Resolution Fluorescence Detection
<b>HXMA:</b>	Hard X-ray MicroAnalysis Beamline
<b>PFY:</b>	Partial Fluorescence Yield
<b>RIXS:</b>	Resonant Inelastic X-ray Scattering
<b>RXES:</b>	Resonant Elastic X-ray Scattering
<b>SOE:</b>	Secondary Optical Enclosure
<b>TFY:</b>	Total Fluorescence Yield
<b>XAFS:</b>	X-ray Absorption Fine Structure
<b>XANES:</b>	X-ray Absorption near edge structure
<b>XAS:</b>	X-ray Absorption Spectroscopy

## LIST OF APPENDICES

<b>Appendix A:</b> Motion Controls for the HERFD System	81
<b>Appendix B:</b> Energy Range of Various Silicon Crystals	83

# 1 Introduction

## 1.1 Project History and Motivation

This project stemmed from an initiative to provide new experimental techniques to produce quality science at the Canadian Light Source (CLS). Specifically, at the Hard X-ray MicroAnalysis (HXMA) beamline where there are currently investigations in two major fields of research, x-ray absorption spectroscopy and x-ray diffraction. The work done in this thesis is an extension of the former looking specifically at x-ray fluorescence data collection and the associated x-ray absorption spectra. The goal of this project is to improve on the conventional x-ray absorption measurements via fluorescence detection mode with the intent of improving the energy resolution of the spectral features. An improved energy resolution would lead to a finer study of the electronic structure of the materials being tested and could result in more conclusive studies.

The method used in this thesis to improve the resolution of fluorescence spectra is not a new concept, in fact it now dates back almost 30 years with the work conducted by K. Hamalainen et. al. in 1991 [1]. The goal when working with a high-resolution fluorescence detector is to achieve an energy resolution that is smaller than the lifetime broadening of the transition of interest [1]. To accomplish this a partial fluorescence yield will be collected as opposed to counting the full fluorescence line, the width of this partial yield in energy space is desired to be on the order of 1-3eV [1]. The experiment fundamentals of this research were to use the Bragg reflection of a curved crystal analyzer

to reflect and focus a small band of fluorescence energy. Some detail on how this is accomplished is outlined below in Section 1.2 with further detail in Section 2.4.

One of the projects that motivated this work was the determination of the chemical speciation of rare earth elements in coal fry. The original scope of this project sought to determine the speciation of lanthanum, cerium, neodymium and ytterbium species for the purposes of extraction. There is currently a large demand for rare-earth elements as well as desire to produce usable materials from a product that would otherwise be waste. If applied HERFD could allow for accurate spectra of these elements in their varying natural states to be used as components in a comparison to the resulting spectra from the coal fry itself. Of course, this is only one example of what would be possible with a system that can produce spectra with such a small energy resolution. For reference the energy resolution of the typical solid-state detector that is used for fluorescence experiments is on the order of 150 eV showing the vast gain in resolution using a HERFD system.

HERFD is now employed widely across the globe with endstations in facilities such as the European Synchrotron Radiation Facility (ESRF) in France [2] and the Advanced Photon Source (APS) in the United States [3]. The work done at APS is one of the driving factors for the development of HERFD at CLS, very positive results were shown in 2018 from the CLS @ APS program that highlighted the spectral improvements gain through HERFD. At the time a HERFD system had not been available to users in Canada for x-ray absorption experiments, leading to Canadian users wishing to use this technique having to travel abroad to gain access.

The goal of this feasibility study was to test the viability of running HERFD experiments at HXMA. It was made possible via a small project initiative supported by the CLS allowing for the acquisition of the various components required for the test system's construction. If the feasibility study yielded positive results this project could simply be the first step in the development of a dedicated endstation at HXMA that would allow users to conduct HERFD experimentation.

## **1.2 High Resolution Fluorescence Detection**

The feasibility study as covered by this thesis will detail the construction and initial testing of a high energy resolution fluorescence detector (HERFD) at the CLS on the HXMA beamline. In this section some detail will be given on this technique and how it provides an increased resolution, for further information see on the background theory see Section 2.3 and 2.4, for additional details on the test systems construction see Section 3.2.

Following the methods of a standard fluorescence experiment, HERFD spectra collection is analogous to a standard x-ray absorption near edge scan, the x-ray beam incident to a sample is scanned across a range of energy while counts in the detector are measured [4]. The difference is the portion of the fluorescence band that is counted over, HERFD is a partial fluorescence yield spectroscopy that seeks to only count over an energy band of approximately 1-3 eV in width [2]. This small energy range is centered on the count maxima of the fluorescence band.

The analyzers that will be discussed and used in this thesis are based on using a crystal analyzer and selecting a Bragg reflection that corresponds to the energy of interest [5]. With fluorescence being a spherically divergent source base construction can follow spherical and cylindrical coordination systems, this thesis will only focus on the spherical case. As such, the crystal analyzers will be spherically bent, the bending radius of the curve can vary based on the arrangement being used (See Section 2.4.1).

The complete HERFD system is constructed on three major components; the sample, the analyzer and the detector. The system used to coordinate these components is a Rowland circle, a coordinating tool used to position the components on an imaginary optical grating [5]. With the correct alignment the sample will absorb the incoming beam resulting in fluorescence emission, the fluorescence will then meet the crystal analyzer where it will be absorbed if it doesn't meet the Bragg condition or reflected if it does. The fluorescence that is reflected will be focused onto the detector where it will be counted. The focusing nature of the bent analyzer crystal should result in a beam spot on the detector the same size as the beam spot on the sample.

The main challenge when working with a HERFD system is ensuring the alignment of all the components as well as selecting the corrected analyzed energy. Much of this thesis will focus on the motor controls, alignment procedures and the energy mapping that is required to ensure the quality of the result.

### **1.3 Overview of Work**

A compact overview of this thesis by chapter is presented below. This will serve as a summary/directory to the various intertwined topics and ideas found within.

Within Chapter 2, background theory and the information that was used when designing and constructing the HERFD system is contained. This included a brief background on x-ray absorption spectroscopy both for transmission and fluorescence experiments. The fundamental background on interpreting and using the resulting absorption spectra for the determination of sample identity, composition and speciation. Focus is then shifted to the theoretical background on improving spectral resolution using a partial fluorescence yield and invoking visualizations based on x-ray emission spectroscopy. Finally, this chapter will discuss HERFD as accomplished using crystal analyzers to selectively focus fluorescence emissions.

In chapter 3, the construction of the test HERFD system is described including motor controls, focusing and scanning routines and the crystal analyzers used. This discussion will include the choice of detector and the specific model numbers of the key components of the system. In addition, details on the HXMA beamline where the test system was operated are provided. Lastly the sample preparation and sample structure are outlined within this section.

Contained in Chapter 4 are the procedures that were followed when running this experiment at the CLS. Specifically, the focusing procedure followed to properly align the optical components onto the Rowland circle. Following this the results of this feasibility

will be discussed and compared to those produced by other HERFD facilities that are currently operating. More specifics on the mapping procedures that would be carried out using this test system and testing done using an alternative geometry are included.

Chapter 5 covers further study and development plans to improve the current HERFD system. Specifically, it will discuss observing the focusing effects of the crystal analyzer, changing the orientation of the HERFD system and extending the range of x-ray energies the system can accommodate. A focus will be put on moving forward from a single crystal test system to the construction of a dedicated HERFD end station with a multi-crystal array. Finally closing remarks will be made on this feasibility study's results and this projects outlook.

## 2 Theory and Background

### 2.1 X-ray Absorption Fine Structure

The experimentation and design conducted within this project fall under the larger field of X-ray Absorption Fine Structure (XAFS) [6]. Generally, this field is split into two regimes based on the x-ray energy range of interest, these regimes are X-ray Absorption Near Edge Spectroscopy (XANES) and Extended X-ray Absorption Fine Structure (EXAFS) these regimes will be expanded on within this section [7][8] .

At its core XAFS is the study of the absorption of incident x-rays by a sample of interest across an absorption edge. An absorption edge corresponds to a large spike in the x-ray attenuation of a given sample [6]. Each absorption edge is associated with a specific core shell electron binding energy of an element in the sample; therefore, this spectroscopy is element specific [4]. For this project the x-rays of interest fall into the lower end of the hard x-ray regime with a wavelength of  $\sim 1.2$  angstrom with relates to an energy of approximately 10 keV.

Absorption spectra and XAFS as a whole can be related to and stem from Fermi's Golden rule. All features seen within a spectrum can be related to a transition rate dictated by a transition operator acting on the initial state of the absorbing atom to produce its final state [8]. The general form of this is shown below in Eqn.1 which outlines the relationship between the linear x-ray absorption coefficient and the transition probability.

$$\mu(E) \propto |\langle f | \hat{e} \cdot \vec{r} | i \rangle|^2 \quad (1)$$

where  $|i\rangle$  is the initial unperturbed state of the absorbing atom,  $|f\rangle$  is the final state and  $\hat{e} \cdot \vec{r}$  is the dipole operator made up of the  $\hat{e}$  the polarization unit vector of the incident x-ray photon and  $\vec{r}$  the electrons location vector [8].

Absorption spectrum intensity (the cross section) is monotonically decreasing unless a resonance condition is met, this decrease is due to higher energy x-rays more easily penetrating media. A resonant condition is met when the incident beam energy is equal to a specific core-electron binding energy in the absorbing atom. In this scenario an incoming photon will be absorbed, and an electron will be excited to the valence band or into continuum; this process causes a spike in absorption. Additional features or intensity modulations in the absorption spectrum come from photoelectron interactions with neighboring atoms [8]. When an electron is excited into continuum it becomes a photoelectron and will be scattered off neighboring atoms. Thus, the spectral intensity modulations hold information on the scattering path of the photoelectron and can be applied to determine the immediate neighboring structure of the absorbing atom [6]. Thus, providing a unique chemical speciation fingerprint.

The distinction between XANES and EXAFS now becomes relevant as these regions provide different information about the sample system. The XANES region is defined as the region up to 50 eV past edge jump and EXAFS is the region beyond this extending into higher energies up to 1 keV past the absorption edge [6].

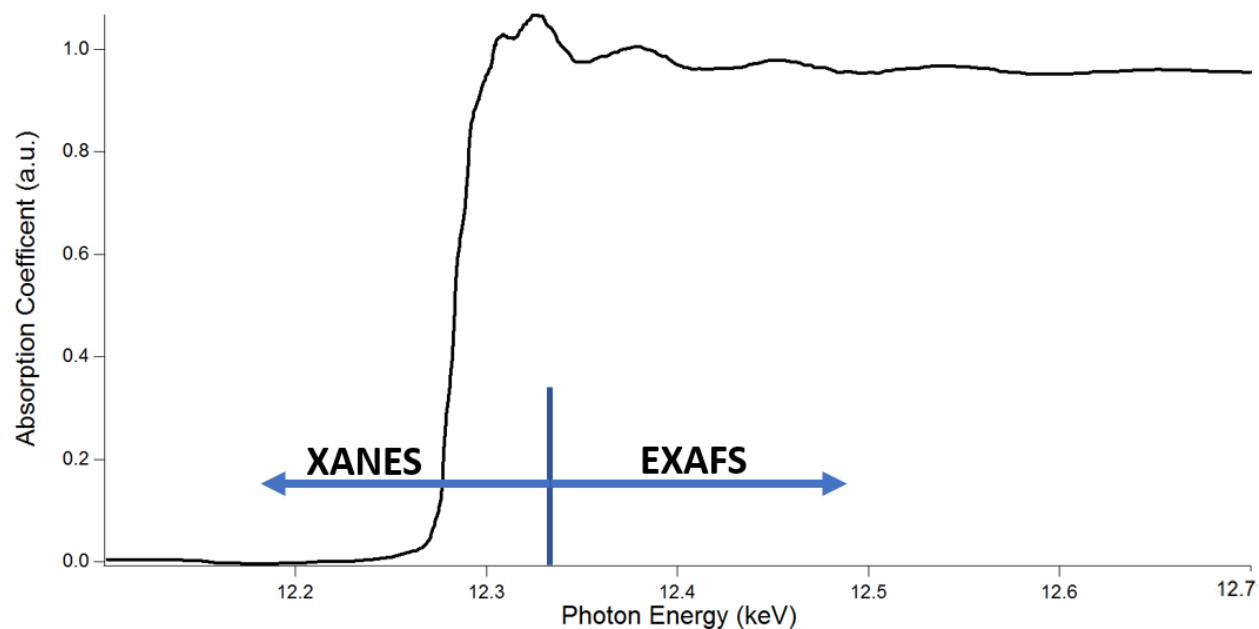


**Figure 2.1:** A normalized absorption spectra of cinnabar mercury sulfide illustrating the boundary between XANES and EXAFS. (The data had it's background removed by a linear fit and was then normalized)

In the XANES region the photoelectron barely has enough energy to escape the absorbing atom's potential well (which is modified by the presence of surrounding atoms) [9]. This makes this portion of the chemical fingerprint very susceptible to molecular potentials created by the symmetry/coordination of neighboring atoms. This high susceptibility further defines a unique fingerprint that can be used to identify materials using a library of know spectra. Alternatively, with a strong understanding of the system first principle calculations can be completed to determine accurate structural parameters. A popular calculation method is known as Finite Difference Method Near Edge Structure (FDMNES) [10].

In the EXAFS region the photoelectron is propelled far beyond the potential well of the absorbing atom. The oscillations found in this region can be attributed to the ejected photoelectron interacting with backscattering electron clouds from neighboring atoms with dominating single scattering features thus creating a sinusoidal interference pattern [7]. Basic approximations of this propagation process use a plane-wave scattering theory however this has largely been retired for a curved wave scattering that includes multiple scattering [11]. From this interference pattern information on the bond length and the number of equivalent scattering atoms at that distance can be extracted, in addition an estimation on the absorbing atom's atomic weight (within 5) can be determined [7].

This thesis will focus on XANES investigations as the increased resolution will be seen about the spectral peaks that fall into the pre-edge and near-edge category. The use of a HERFD system offers minimal gain in the EXAFS energy regime.

## **2.2 XAFS Instrumentation Basics**

To complete a XAFS investigation one requires a scannable monochromatic x-ray source, often obtained from an insertion device x-ray source in a synchrotron radiation beamline facility [12][13]. The beam produced by an insertion device will carry a finite bandwidth of x-ray energies/wavelengths; therefore to conduct XAFS measurements it must be passed through a monochromator to select a single x-ray energy [5]. For this investigation a synchrotron beamline with a wiggler and a double crystal monochromator was used. Fundamentally the wiggler produces x-ray photons by deflecting a beam of electrons back and forth transverse with respect to the electron propagation direction

inside the synchrotron's storage ring. This deflection is accomplished using an alternating magnetic array [13]. The change in acceleration caused by the magnetic deflections produce a broad spectra of x-ray photons tangential to the curve of the synchrotron storage ring [12]. This spectrum of x-rays is then collimated and passed to the monochromator. The monochromator reflects a selected x-ray energy/wavelength by Bragg diffraction. A second parallel crystal of the same cut will allow for a fixed exit height for the reflected x-rays.

Once the monochromatic x-ray beam is established its intensity/photon flux must be measured, this is generally done using an ionization chamber filled with inert gas such as helium or argon (depending on the energy range). The use of such a detector allows for minimal intensity loss during the detection process ensuring the maximum flux is maintained.

With the incoming intensity determined the beam will then reach the sample which will either be situated normal to the beam for transmission detection or typically at a  $45^\circ$  angle to the beam for fluorescent detection. The proceeding optical arrangement from the sample will depend on the chosen detection mode. For this investigation, fluorescence will be the focus, however, a brief overview of both modes can be found below.

### 2.2.1 Transmission Mode

A basic transmission experiment would use a second ionization chamber to measure the beam after it has passed through the sample allowing for the transmitted intensity to be measured. There will often be a reference sample and third ionization chamber following  $I_1$ , this allows for an energy calibration and reference spectra to be taken concurrently with the scan of interest. This arrangement is illustrated in Figure 2.2.

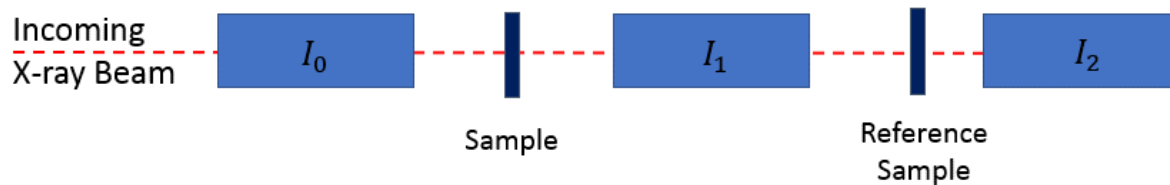


**Figure 2.2:** Schematics of a typical set-up for a transmission mode measurement, using three ionization chambers to measure the absorption of an unknown and a reference sample

The data obtained from the two ionization chambers ( $I_0$  and  $I_1$ ) is used for calculations relating to the exponential attenuation of photons through the sample as dictated by:

$$I_1 = I_0 e^{-\mu x} \quad (2)$$

here  $x$  is the thickness of the sample and  $\mu$  is the linear x-ray absorption coefficient [6]. A properly prepared sample is required to be adequately thin and uniform such that it does not introduce self-absorption effects or other spectral artifacts. As a standard, samples are prepared to have a thickness of approximately  $\frac{1}{\mu_{edge}}$  where  $\mu_{edge}$  is the absorption coefficient at the edge energy [6]. The natural log of Eqn.3 follows to be:

$$\mu x = \ln \left( \frac{I_0}{I_1} \right) . \quad (3)$$

Here  $x$  can be normalized out; further simplifying the equation. Using this, an absorption spectrum is generated by measuring incoming and transmitted beam intensities while scanning through an incoming x-ray energy range of interest.

### 2.2.2 Fluorescence Mode

In contrast to the transmission detection mode, which measures the remaining beam after passing through the sample, fluorescent detection measures the intensity of a secondary x-ray photon. This photon is produced through a two-step process; absorption and relaxation. First the absorption of an incoming photon which will excite a core-shell electron into the valance of the atom or continuum leaving a hole in the shell it originated. The presence of the hole makes the atom unstable as it is in an excited state. To regain stability the hole will be filled by an electron from a higher energy shell via the relaxation process. The movement of the electron from the higher shell to occupy the core-hole can

release/emit a photon with energy equal to the difference in energy between the two shells. These emitted photons will be spherically divergent as they leave the sample. A visualization of the fluorescence process can be seen in Figure 2.3, this figure depicts an initial k-shell excitation however an electron hole can be produced in any shell.

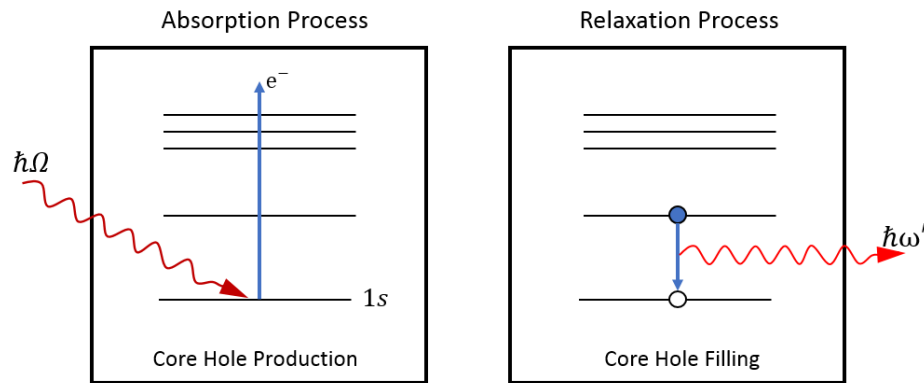


**Figure 2.3:** Fluorescence photon production through x-ray absorption that creates a core-hole via a K-edge excitation

To produce fluorescence results that can be taken as an equivalent to an absorption spectrum, one of two sample conditions must be met. Either the sample must be prepared to be dilute (on the order of 0.1-1% by mass) or as a thin film, this avoids self-absorption and enables the approximation made in Eqn.4 [6].

$$\frac{I_f}{I_0} \propto \mu(E) \quad (4)$$

Thus, given the above sample requirements are met the fluorescence generation process will be proportional to the x-ray absorption coefficient [6]. That is the secondary photon intensity ( $I_f$ ) can be used to measure the absorption coefficient. Thus, with the proper sample preparation analysis can be completed through measuring incoming and fluorescence intensity through a continuous energy range of interest. Once again normalization on the resulting data will be required prior to analysis.

In a basic fluorescence optical arrangement, the sample is mounted to have an angle of  $45^\circ$  with respect to the incident beam. The detector will face the sample and be placed perpendicular to the beam, this arrangement is illustrated below in Figure 2.4. There are a variety of viable detectors for fluorescence experiments including solid state, Lytle and hybrid pixel-based detectors. Detector selection should be based on the samples of interest and experimental goals. A common trait that these detectors must share is the ability to measure the same amount of solid angle produced from the fluorescence emission for the entirety of the incident energy scan.

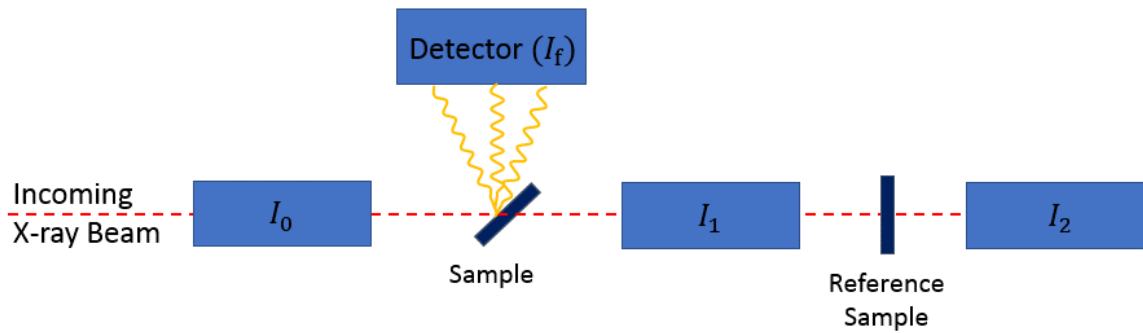


**Figure 2.4:** Schematic of a typical experimental set-up for a fluorescence mode measurement, using three ionization chambers to measure incident intensity and the absorption of a reference sample. In addition, a fourth detector is used to measure fluorescence intensity

## 2.3 Improving Fluorescence Resolution

The purpose of this thesis was to develop a prototype apparatus that can be categorized as a High Energy Resolution Fluorescence Detection System (HERFD) [1], [2], [4], [14]–[18]. A HERFD XAS system seeks to improve the energy resolution of spectra by improving the spectral sharpness. This is accomplished by limiting spectral broadening. Thus, to attain HERFD spectra, measurements must have a higher resolution than the energy spread due to core-hole lifetime [14]. The core-hole lifetime is contextualized by the Kramers-Heisenberg formula which dictates the probability/intensity of a fluorescence emission. The full form of this equation can be seen below in Eqn.5 [18].

$$I(\Omega, \omega') = \sum_j \left| \sum_m \frac{\langle j | \hat{\varepsilon}' \cdot \vec{r}' | m \rangle \langle m | \hat{\varepsilon} \cdot \vec{r} | g \rangle}{E_g + \hbar\Omega - E_m - i\Gamma_m/2} \right|^2 \frac{\Gamma_j/\pi}{(E_j + \hbar\omega' - E_g - \hbar\Omega)^2 + \Gamma_j^2} \quad (5)$$

This form of Kramers-Heisenberg is for a general fluorescence production, the intensity of emitted photons for a set incident ( $\hbar\Omega$ ) and fluorescent energy ( $\hbar\omega'$ ). Here  $g$  is the unperturbed state of the atom,  $m$  is the excited state with the initial core-hole created from an absorption and  $j$  is the state once an electron from a higher shell fills the initial core-hole (leaving a new core hole in a higher shell). The two  $\langle m | \hat{\varepsilon} \cdot \vec{r} | g \rangle$  expressions are the initial state (eg.  $|g\rangle$ ) being acted on by a dipole operator to transition to the final state (eg.  $\langle m|$ ). Beyond this,  $E_g, E_m$  and  $E_j$  represent the binding energies of the associated orbitals. Finally, the  $\Gamma_m$  and  $\Gamma_j$  are the lifetime broadenings of intermediate states. These broadenings are important as they dictate the spread a resonance condition will occupy in energy space. This concept will be developed and outlined in section 2.3.1 with the aid of RXES mapping as a tool to visualize these quantities.

However, for this thesis the general form of Kramers-Heisenberg can be simplified to only  $L_3$  edges as the fluorescence photons of interest are  $L\alpha_1$  [14]. Using this information Eqn.5 can be simplified to equation Eqn.6 by allowing  $m$  to be set to  $2p$  and  $j$  be set to be a  $3d$  hole (holes within a shell will be denoted as the shell with an underline). In addition, this simplified form is visualized in Figure 2.5 showing the movement of electrons and the initial, intermediate and final state.

$$I(\Omega, \omega') = \sum_{\underline{3d}} \left| \frac{\langle \underline{3d} | \hat{\epsilon}' \cdot \vec{r}' | \underline{2p} \rangle \langle \underline{2p} | \hat{\epsilon} \cdot \vec{r} | \underline{2p} \rangle}{E_{\underline{2p}} + \hbar\Omega - E_{\underline{2p}} - i\Gamma_{\underline{2p}}/2} \right|^2 L_{\underline{3d}} \quad (6)$$

In addition, within this form of the equation  $L_{\underline{3d}}$  is introduced, this term is a convolution of the energy conservation term seen in Eqn. 5, it also contains the final state lifetime broadening. This convolution is often separated from the leading sum as resulting apparent lifetime broadening calculations will be dominated by the intermediate state lifetime.

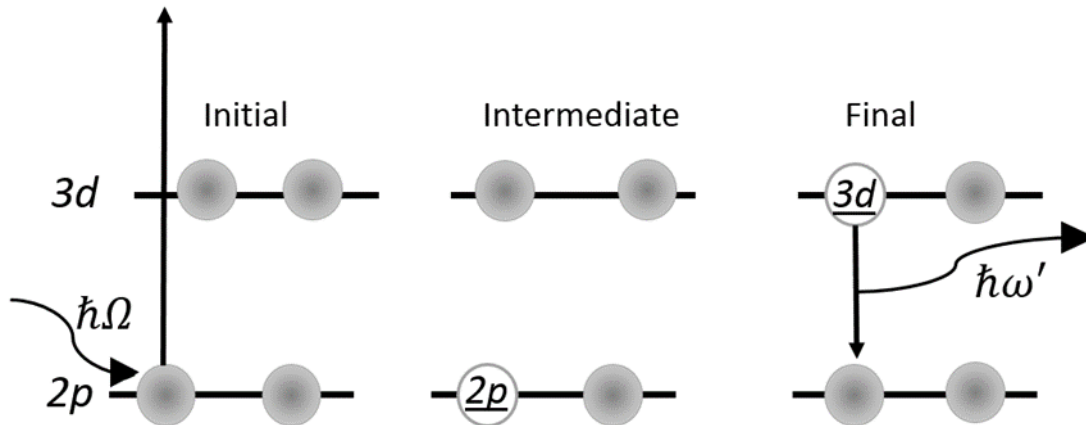


**Figure 2.5:** The fluorescence process of an L3 excitation resulting in a 2p hole that will be filled by a 3d electron, the movement of the 3d electron will release an L $\alpha$  photon as the fluorescence emission

A visualization of the lifetime broadening, and core-hole lifetime can be taken from resonant x-ray emission techniques. Specifically, RXES mapping from which an energy

convolution can be taken to gain an estimate for the apparent core-hole lifetime. This discussion can be found in section 2.3.1.

In addition to lifetime broadening another factor that is important to spectral sharpening is the energy spread of a transition. Energy spread comes from the energy separation found within a single orbital/shell. The energy separation of different states within a single orbital is larger in lower shells. Due to this separation, an electron transition from a higher shell to a hole in the lower shell will result in a larger range of emitted fluorescent energies [4]. So, in general transitions involving higher orbitals will be sharper due to the less variance within their energy band. Thus, there is a draw to investigate these resonances.

### **2.3.1 Resonant X-ray Emission Spectroscopy Methods and Mapping**

Resonant x-ray emission spectroscopy (RXES) is another synchrotron radiation-based spectroscopy technique that looks at electron excitation to the valence of a sample via absorption [19]. RXES is a photon in – photon out spectroscopy that is interested in the emission intensity as a function of the energy transfer that takes place within the system [19]. RXES gains its name from choosing an incident energy that will match with an x-ray absorption edge energy of the sample thus meeting a resonance condition. RXES can be split into two subgroups based on if it is an elastic or inelastic absorption-emission process. this thesis is interested in the inelastic portion of RXES known as Resonant Inelastic X-ray Scattering (RIXS).

RIXS follows the same process as explained above by the Kramers-Heisenberg formula where a core electron is excited to the valence band (this excitation can be drawn as a parallel to the XANES region of XAFS). Following this, the atom has entered its intermediate state, where there is an additional valence electron and hole in the core level. In some cases, there could be many electron transitions required to fill a core-hole as an electron cascade occurs shifting the electron hole up into higher shells. Each transition would either release a fluorescent photon or involve other electronic processes such as Auger electron emission [7]. The release of a fluorescent photon can be associated with a Ramen shifted feature that is tied to the given transition. This thesis focuses on resolving the features of a single Ramen shifted feature, specifically the emission from a mercury  $3d$  electron filling a  $2p$  hole.

RIXS in general can be used to probe many different features of system including density of states, band gaps, ect [19]. However, as this thesis is concerned, only the concept of a two-dimensional contour map of fluorescence intensity as a function of transfer energy and incident energy is relevant. Within these maps, energy transfer ( $\hbar\omega$ ) is defined as the difference between the incident photon energy ( $\hbar\Omega$ ) and the emitted photon energy ( $\hbar\omega'$ ) [19].

$$\hbar\omega = \hbar\Omega - \hbar\omega' \tag{7}$$

A visualization of RIXS maps plotted as function of emitted energy and energy transfer can be seen in Figure 2.6. The sizes of a RIXS map are small on the order of  $\sim 20$  eV this means in a standard fluorescence measurement all counts/intensity seen within the map will be included [19]. This is due to standard fluorescence detectors only having an energy resolution of  $>100$ eV. So, it is impossible to discern between different points with a vertical point on the RIXS map. Therefore, all photons associated with a given Ramen shifted feature will be integrated in a typical count. The goal of HERFD XAS is to attain an energy resolution on the order of 1-5eV such that one can take spectra that count over a small subset of the area within a RIXS map. How this is accomplished is outlined in Section 2.4.

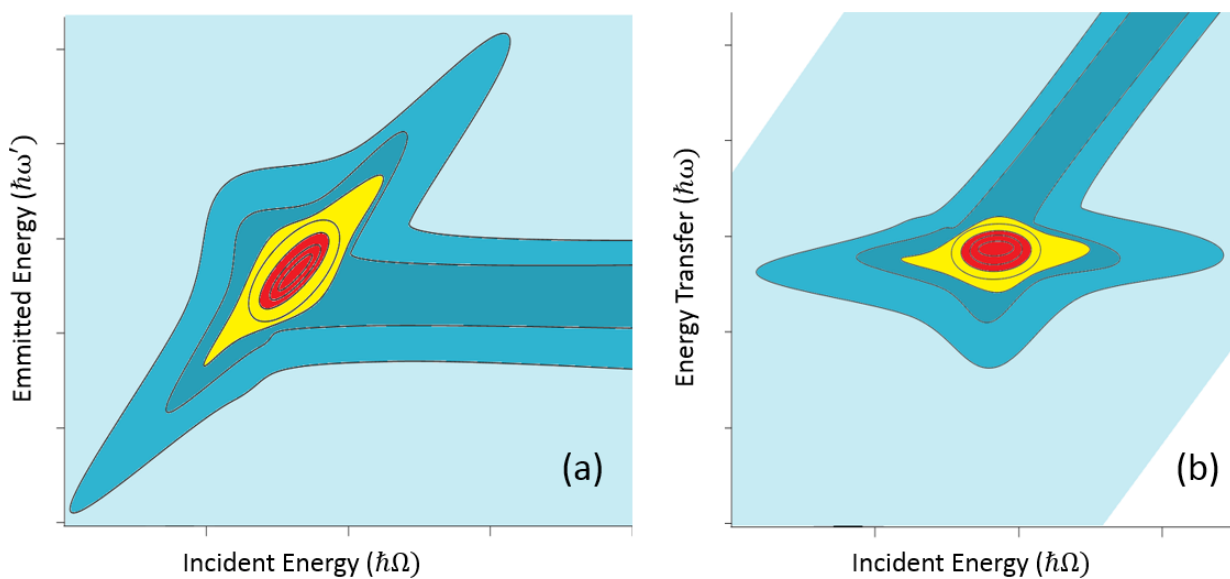


**Figure 2.6:** Schematics of the same RIXS map plotted using the two different axis conventions the scale in both cases is on the order of 20 by 20 eV. The map shown labeled (a) shows the rough shape of a Ramen shifted feature in emitted vs incident energy space, in(b) the vertical axis is shifted to energy transfer

space. In energy transfer maps a line of constant emitted energy will be diagonal with a slope of 1. Describe the typical scale of such maps.

A benefit of RIXS mapping for HERFD purposes is the ability to extract the lifetime broadening of a resonance based on the space it occupies in the RIXS map [4], [14]. This is gained through doing a convolution of the energy peak width in both direction and using Heisenberg's uncertainty principle resulting in:

$$\Gamma_{app.} = \frac{1}{\sqrt{\frac{1}{\Gamma_{int.}^2} + \frac{1}{\Gamma_{fin.}^2}}} \quad (8)$$

Here  $\Gamma_{app.}$  is the apparent lifetime broadening of a transition,  $\Gamma_{int.}$  is the lifetime broadening of the intermediate state and  $\Gamma_{fin.}$  is the final state broadening [14]. The atomic state designations (initial and final) for these lifetime broadenings are referring to those described in Figure 2.5. It is again important to note that this equation will be dominated by the intermediate state lifetime, as it is much smaller than the final state lifetime. For reference, the core-hole lifetime broadening of liquid mercury for the  $L_3 - M_5$  transition (the transition of interest for this thesis) is  $\sim 9$  eV [20].

The apparent lifetime broadening of a transition is the barrier which a HERFD system must overcome as the system resolution must be less than the lifetime

broadening. This introduces a limitation on what transitions a given HERFD system can successfully run based on its achievable resolution.

## **2.4 High Energy Resolution Fluorescence Detection**

The high energy resolution detection (HERFD) system used in the context of XAS was introduced by K. Hamalainen et. al. in 1991 who established this technique with the intent of eliminating the inner-shell lifetime broadening to increase spectral sharpness [1]. To accomplish this, a Bragg diffractive optical arrangement was used, the structure and functionality of this type of arrangement can be found in detail within section 2.4.1.

The purpose of the Bragg arrangement was to act as an analyzer on the fluorescent photons that in an ideal scenario would only reflect photons of a single energy to the detector [1]. In practice the analyzer will reflect a small range of photon energies generally on the order of 1- 5 eV. This energy range could be selected through geometric adjustments, the goal being to select the analyzer energy that correspond to the count maxima of the chosen fluorescence band [1]. Ultimately this allows for only a small portion of the fluorescence band to be counted instead of taking the total fluorescence yield (TFY), making HERFD a partial fluorescence yield (PFY) spectroscopy [1].

The width in emission energy of a given fluorescence band is on the order of 20 eV, further demonstrating a conventional fluorescence arrangements inability to conduct this PFY. Given a HERFD system functions with a resolution of 1-5 eV, the PFY that is counted will appear as a narrow band about the count maxima of the fluorescence band, this is visualized in Figure 2.7.

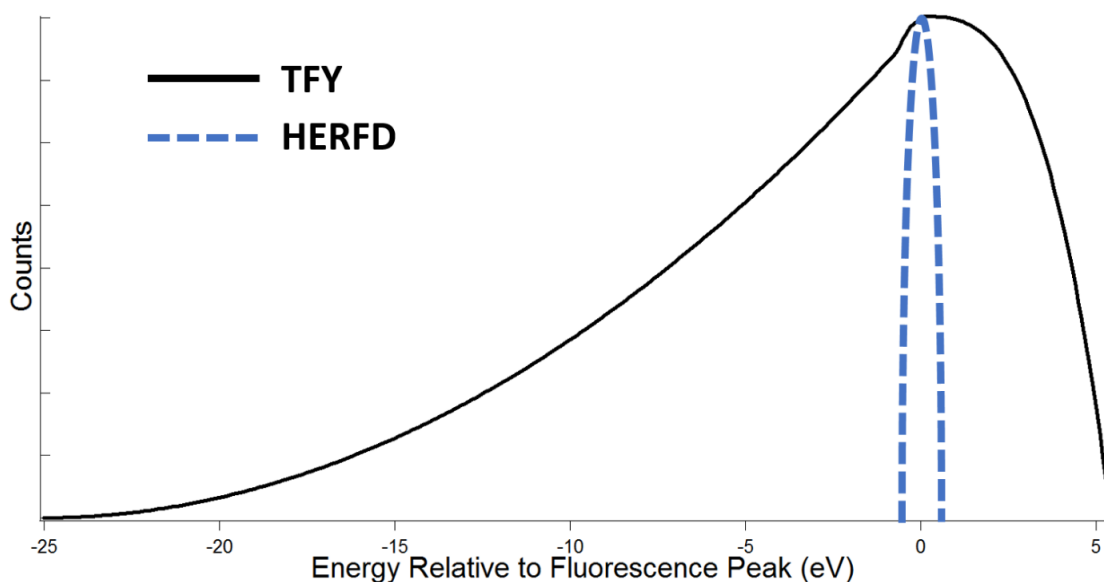


**Figure 2.7:** A schematic view of a standard fluorescence band at a given incident energy will be fully integrated over in a standard fluorescence experiment, HERFD seeks to only integrate over a small portion the band as highlighted by the blue dashed line. The width of the HERFD counting region shown within this figure is an idealistic case with a 1eV analyzer resolution.

Thus, a HERFD XAS scan consists of measuring counts at a constant emission energy while varying the incident energy. This scan can be overlaid onto a RIXS map to provide a visualization of the scan in energy space and with respect to resonance features. This appears as a thin band of constant emission energy crossing the peak of the resonance feature (see Figure 2.8). This type of contour plot visualization was completed by F. M. F. de Groot et. al in 2002, while improving spectra of platinum L edges [14]. Within a RIXS map plotted as transfer energy against excitation energy, a HERFD scan presents as a diagonal line across the maxima with a slope of one. The width of this line is determined and limited by the resolution of the system. In Figure 2.8 a schematic

view of a HERFD scan in RIXS space showing the portion integrated as well as the difference in peak width between a HERFD and standard fluorescence scan.

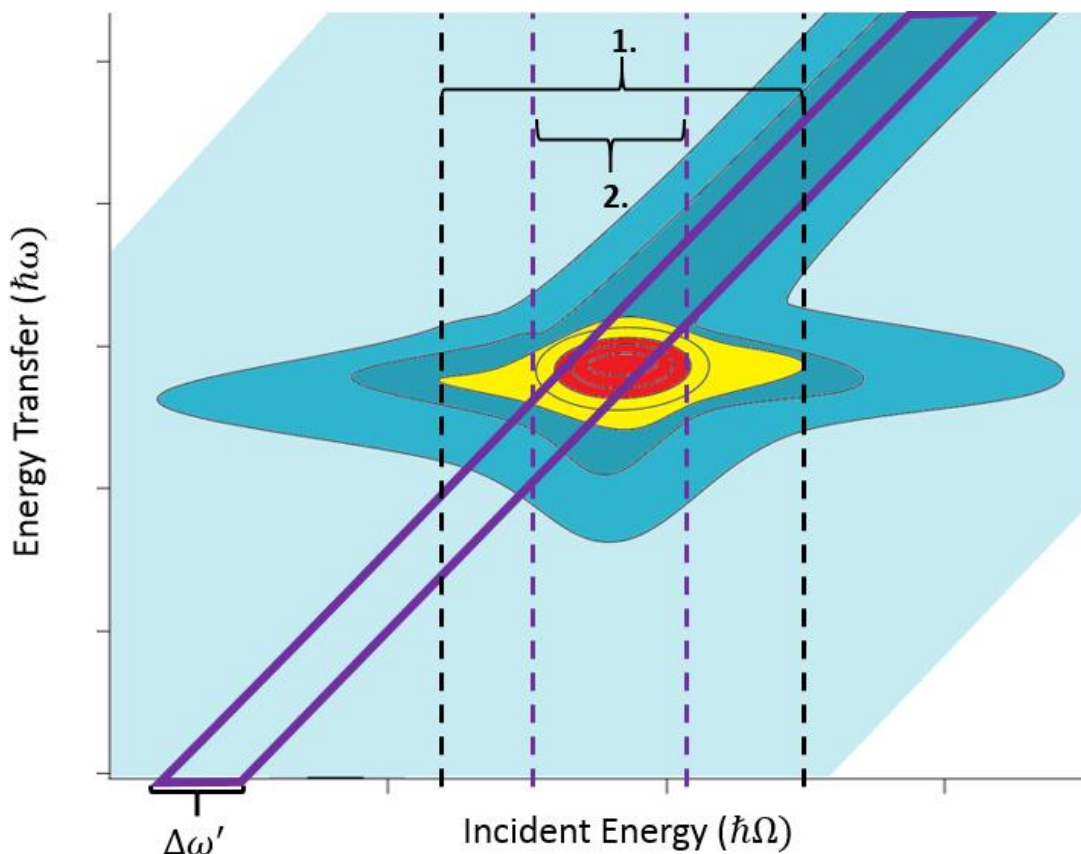


**Figure 2.8:** The purple rectangle displayed on this RIXS map represents the portion of fluorescent photons that HERFD collects, the width the rectangle corresponds to the accuracy in the analyzed energy reflected from the crystal analyzer. The width between dotted lines represents, how wide the peak will be seen in the absorption spectra. The width marked with 1. is the peak width for conventional fluorescence detection and the width marked with 2. is the peak width for HERFD collection. This depicts the increased sharpness gained from a HERFD scan.

When viewing a RIXS map of energy transfer vs. incident photon energy the PFY of a HERFD scan can be viewed as a projection onto the incident energy axis producing the

resulting absorption spectra. The HERFD spectra thus gets its sharpness by not convoluting and smearing its features with background counts and the periphery of the resonance. So, while all features are technically present in a TFY experiment they will be muted in comparison with some showing no definition at all.

The usefulness and ability of a HERFD system hinges on the analyzer/mechanical resolution. Complications can arise based on the sample of choice, where other resonance features may overlap, or aberrations arise. For this reason, when working with an unknown system completing even a low-quality map is beneficial to ensure all features seen in the final HERFD spectra can be attributed to the single resonance. The method of completing such a map is expanded in section 2.4.2. This thesis will not detail the other aberrations and their source, for inquiries and clarification see [5], [21].

#### **2.4.1 Bragg Reflective Fluorescence Detection**

As mentioned earlier high-resolution fluorescence detection doesn't measure direct fluorescence, instead the emitted fluorescent rays are first reflected by a crystal analyzer. The analyzer is usually a silicon or germanium wafer cut to have a chosen Bragg plane parallel to its surface. This plane will reflect the fluorescent photons as governed by Bragg's law:

$$n\lambda = 2d \cdot \sin\theta \quad (9)$$

here  $\lambda$  is the wavelength of reflected photons,  $n$  a positive integer,  $d$  is interplanar distance and  $\theta$  is the angle the photons meet the crystal surface at. The crystal cut/Bragg plane is selected based on the desired photon energy range one wishes to reflect. Bragg angles approaching  $90^\circ$  are desired for reasons that will be discussed later in this section. Within this energy range, the angle of the crystal relative to the x-ray source can be adjusted to select the exact analyzer energy of interest. Allowing for only the selected energy and its associated harmonic energies (allowed via varying  $n$  values) to be reflected and filtering out/absorbing all signals not meeting the Bragg condition.

The inherent energy resolution of this process is dependent on the Bragg angle between the sample and crystal analyzer, this resolution is given by the equation below where interplanar distance has been taken to be a constant.

$$\frac{\partial E}{\partial \theta} = \frac{nh}{2d} \cot(\theta) \csc(\theta) \quad (10)$$

From Eqn.10 it is apparent that the higher the Bragg angle is the more optimized the energy resolution of the system will be. This introduced an angular limitation on the crystal analyzer when trying to maintain high energy resolution results. Thus, a variety of different crystal cuts are required to cover large sections of energy space while only taking scans that maintain a Bragg angle well over  $70^\circ$ . This is also the upper limit of the energy resolution a crystal can provide as it doesn't account for any imperfections in the crystal bulk or deformations from the desired curvature.

HERFD XAS measurement is a photon hungry process as it requires a secondary emission and then further rejects a large portion of the fluorescence band all of which is being produced by a spherically divergent source. Flat crystal analyzers are limited in the amount of solid angle they can cover while maintaining the desired Bragg angle. Thus, the crystal analyzers are required to be curved allowing for more solid angle coverage and resulting in a more time efficient system. Due to these requirements a typical crystal will be spherically or cylindrically curved. The size and curvature of these crystals will be further outlined in section 2.4.1.1.

#### **2.4.1.1 Johann, Johansson and Von Hamos Geometry**

Based on the spherical nature of fluorescence emission a circular/spherically oriented analyzing and detection system become an obvious choice. These arrangements are constructed from a Rowland Circle which is simply a circular optical grating to be used as a coordination system for the optical components [5]. The components of the optical system discussed in this thesis are the sample stand, crystal analyzer and detector. Within these geometric systems the Rowland circle is coordinated such that it is tangential to the center point of the crystal analyzer [5]. From this base alignment several geometries are built. This thesis will address two spherical geometries and one cylindrical which are discussed below.

**Johann Geometry:** A geometric arrangement centered about a spherically bent crystal analyzer with a radius twice that of the Rowland circle on which it is placed [5]. This is displayed in a schematic diagram of Johann geometry be seen in Figure 2.9. The

sample and detector can be moved along the Rowland circle to satisfy a specified Bragg angle with respect to the crystals center. The crystal holding a larger bending radius than the Rowland circle radius allows approximately the same Bragg reflection to be maintained across its surface. However, as the crystal grows larger there will be a deviation from the selected Bragg angle at its edges which leads to a small energy range being reflected rather than a singular energy [5]. Reflecting a range of energies inherently lowers the resolution of the system so in order to avoid a loss in resolution there is a maximum size limit per crystal and as such a multi-crystal array may be required to provide adequate signal.

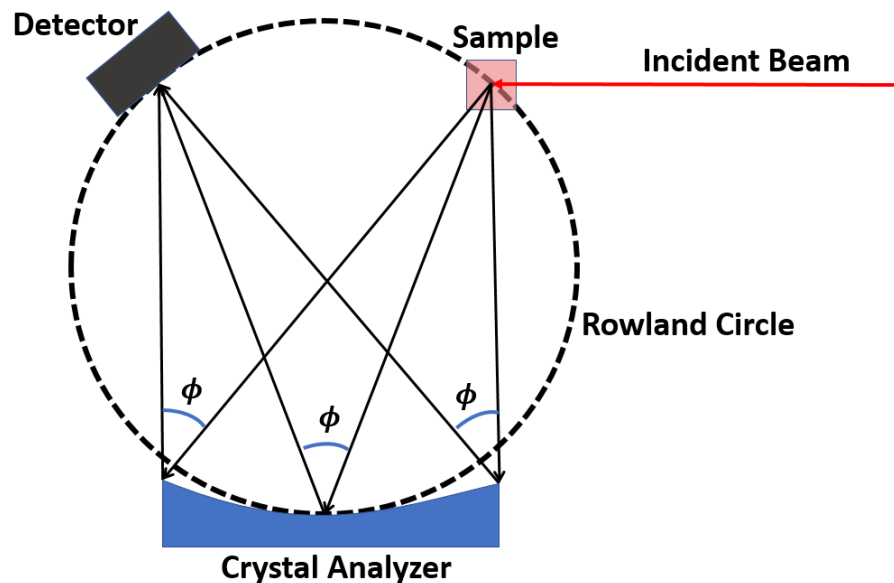


**Figure 2.9:** An illustrative visualization of Johann geometry showing the larger bending radius of the crystal analyzer and beam/fluorescence path. The size of the crystal shown is exaggerated to illustrate its ability to hold relatively the same Bragg angle to the sample across its surface. For visual clarity the angle depicted is twice the complement of the Bragg angle  $\phi$ . ( $\phi = 2[90 - \theta]$ )

**Johannsson Geometry:** Shares the same structure as Johann geometry, the distinction comes from a change in the crystal's curvature. After being bent to have a radius twice that of the Rowland circle as in Johann structure the crystal surface is then ground till it's curvature is the same as the Rowland circle [5]. This negates the issue from Johann geometry where the apparent Bragg angle at the edges of the crystal is not the same as the center. However, there is also more risk in producing crystals using this method as deformation can occur in the grinding process and aberrations and imperfections may arise.

**Von Hamos geometry** makes use of a cylindrically bent crystal analyzer. It still uses the basis of a Rowland circle; however, now there is a vertical displacement between the sample, crystal and detector [22]. Within this geometry the image projected onto the detector by the crystal analyzer will be energy resolved. This is due to the fluorescent waves meeting the cylindrical crystal with significantly different Bragg angles depending on the vertical coordinate of reflection [22]. As such, a shorter and wider crystal is preferred to maintain a level of fluorescence counts that are measurable. In addition, this arrangement would require multiple solid-state detectors on a pixel-hybrid detector to measure the energy resolved emissions while maintaining a high resolution. This introduces an inherent cost increase and leads to detection complications making this geometry unsuitable for the feasibility study in this thesis.

## 2.4.2 Energy Mapping Using a Johann Bragg System

This section will outline how to create a RXES map using a Johann HERFD system. While this won't provide the same resolution of a dedicated RXES endstation, it is a technique that is required to fully understand a sample and ensure proper data collection. It is also important to note that mapping is a large time investment as many scans are required to complete a single map. However, the typical map used for a HERFD investigation is under 30eV by 30eV, so individual scans can be taken quickly; however, mechanical adjustments/movements are required for each analyzer energy slowing the scanning process and ultimately requiring automation.

Mapping requires an incident energy scan for various analyzed energies to propagate the map. Each scan will correspond to a diagonal line up and across the transfer energy RIXS map. Geometrically this requires a set of scans at slightly different Bragg angles progressively populating the map one line at a time. Fixing the sample in place, this will require the detector and analyzer to move; this movement can be viewed as shifting the Rowland circle about the sample as seen in Figure 2.10. With two cartesian degrees of freedom on the analyzer and detector this is easily accomplished through adjustments parallel and perpendicular to the beam.

However, as this is a rough mapping and for a feasibility study, one may wish to limit the degrees of freedom required for these adjustments. For the small region that the Bragg angle must shift to cover the fluorescence maxima a single stage linear motion on the analyzer and detector will suffice. As the Bragg angle increases the detector is

required to move linearly away from the sample, the analyzer will move towards the sample and further down the beam path at a fixed angle relative to the beam. This angle as well as the distance traveled between subsequent scans is dependent on Bragg angle at the fluorescent line's maxima.

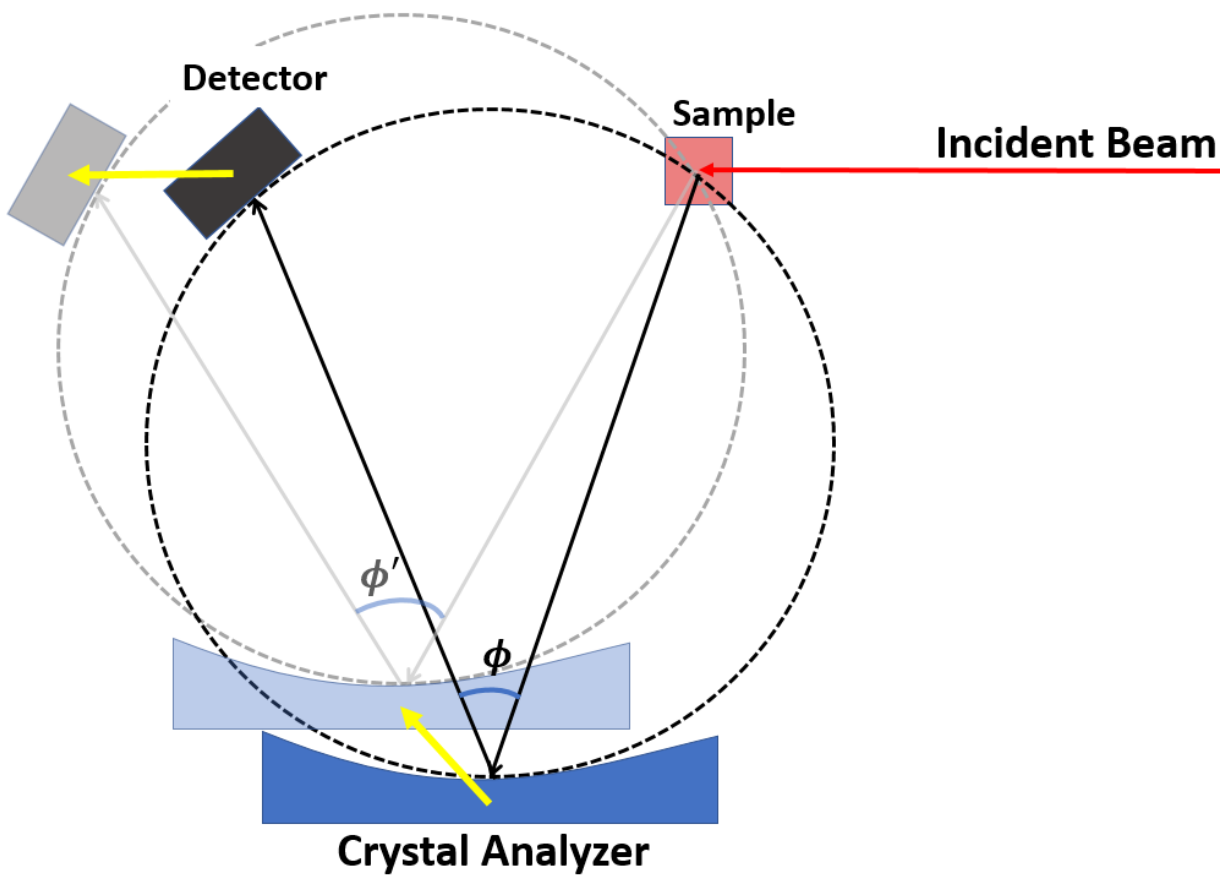


**Figure 2.10:** The movements required for an adjustment to a higher analyzed energy are shown by the yellow arrows. This can be viewed as a rotation of the Rowland about the sample's location. This represents a decrease in Bragg angle and thus an increase in the allowed reflected energies

## 3 Instrumentation and Construction

### 3.1 Canadian Light Source: HXMA Beamline

All experimentation for this thesis was completed at the Canadian Light Source Inc., Saskatoon, SK (CLS) on the Hard X-ray Micro-Analysis (HXMA) beamline. The CLS features a synchrotron which uses an electron gun followed by a linear accelerator and booster ring to accelerate electrons to 2.9 GeV. These electrons are then injected into the storage ring creating a circulating current of 250 mA, this current will decay over time and once it reaches 150 mA the ring will undergo another electron injection to increase current back to 250 mA. The HXMA is an insertion device beamline that uses a sixty-three-pole superconducting wiggler (nominal field strength of 2 T) to produce a broad band (“white”) x-ray beam [23]. Beyond the wiggler the beamline uses a two-hutch system with the primary optical hutch followed by the experimental hutch.

The goal of the primary hutch is to provide a beam that is point-focused and monochromatic to the experimental hutch at a fixed elevation with a selected photon energy in the range 5-40 keV. Within the primary optical hutch, the white beam is trimmed in size (ca. 1 mm x 6 mm) using a set of x-ray slits (referred to as white beam slits, or WS). The beam is then collimated by passing through a 1.2 m long silicon water cooled cylindrical collimating mirror producing a parallel collimated beam (going towards the monochromator). Following this the collimated beam will enter a double crystal monochromator which is equipped with two sets of silicon crystals to be selected based on the energy range of interest (Si(111) and Si(220)). For this investigation the Si(111)

was selected for its aptitude in the energy range of interest (~12 keV). Finally, the beam will enter a toroid-mirror prior to the experimental hutch, this mirror serves to focus the beam to a point. Ultimately the beam that leaves the primary optical hutch will be in-plane linearly polarized, at a fixed energy and point focused.

Upon entering the secondary optical hutch, the beam is passed through a set of monochromatic beam slits (by the trade name JJ™, [24]) to set the beam size with which it will reach the sample. For this experiment the incoming intensity of the beam was measured using an ionization chamber filled with helium gas. The design and alignment of the sample remaining optical arrangement is to be described in section 3.2 and is the portion of equipment unique to this experiment.

The remaining information about the beam, which is important to note as it reaches the sample is its divergence and photon flux. The beam entering the secondary hutch is convergent meaning the beam spot on the sample will be marginally smaller than that set by the JJ slits. The photon flux is relevant when comparing the incident photon count to the photon count yield of the HERFD signal. For a 1 mm by 1 mm beam at HXMA the incoming count rate is approximately  $10^{12}$  ph/s/0.1%Bandwidth [23]. This is one of the limiting factors on the attainable HERFD signal when using a wiggler beamline as opposed to an undulator beamline where the brilliance of the beam is approximately a hundred times higher. ( Brilliance is  $\frac{\textit{photons}}{\textit{second} \cdot \textit{mrad}^2 \cdot \textit{mm}^2 \cdot 0.1\%BW}$  which translates to the photon flux normalized in phase space; the higher the brilliance the higher the monochromatic counts)

## 3.2 Design and Construction

The geometry chosen for this feasibility study was selected based on a set of space, cost and mobility constraints. The goal was to create a small and mobile system that could be used at any beamline that wished to run this testing. In addition, it would use a set of detectors already available in the equipment pool at CLS: HXMA. Based on these constraints the HERFD arrangement was chosen to be a horizontal Johann system built on a movable platform. The platform could then be mounted on any optical table using standard guide rails. This would allow for the system to be fully self-contained with the essential Rowland circle geometry pre-established independently from the beamline on which it is used. The large caveat to this mobility is the need for the alternate beamline to accommodate the driving chains (power supplies and control electronics) for the stepping motors required for analyzer energy adjustments and mapping, the motors used for this will be described later in this chapter.

The Johann system was constructed around a spherically strip bent spherical crystal analyzer with a curvature radius of a 0.5 m, thus necessitating the Rowland circle to have a 0.25 m radius. Within this circle one can envision an isosceles triangle connecting the sample to the center of the crystal then back to the detector, this can be seen in Figure 3.1 which is drawn to scale for sample, analyzer crystal and detector dimensions; the beam shown is oversized to allow its visualization. In the following subsections a detailed overview of the key elements of this optical arrangement will be described as well as the control systems used to adjust their positioning.

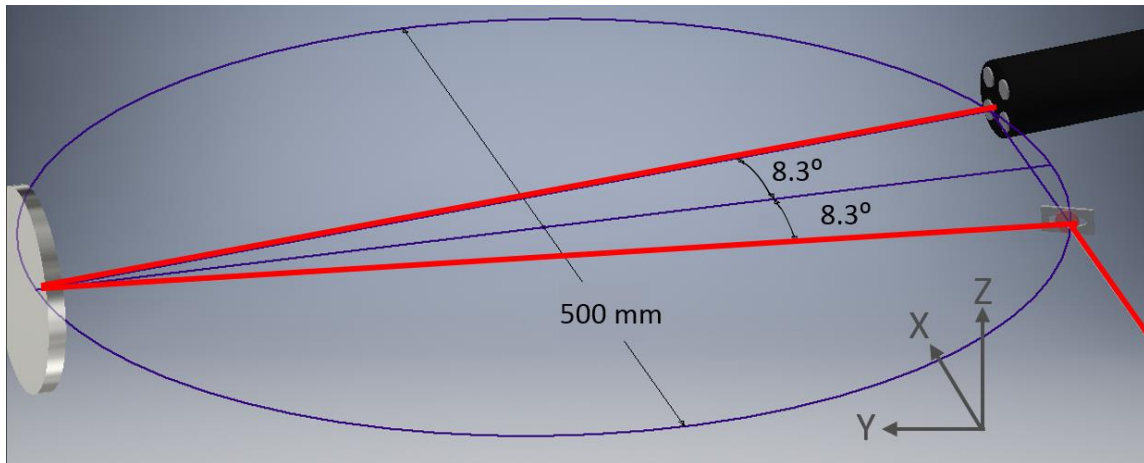


**Figure 3.1:** A schematic diagram showing the scale and arrangement of the sample, crystal analyzer and detector, respectively, on the Rowland circle. Also shown is the incident beam and the path of fluorescence from the sample to the analyzer and reflected to the detector.

### 3.2.1 Spherically Bent Silicon Crystal Analyzer

The crystal analyzer is the crucial component of the HERFD system as it is the component that allows for a narrow band of analyzed energy to be reflected leading to the increase in energy resolution. The crystal analyzer used for this thesis was produced by XRS TECH LLC. [25], it is composed of spherically bent silicon wafer strip cut and mounted on a glass backing. The crystals diameter was 100 mm and was comprised of six strips sliced on a single silicon wafer (Fig.3.3). The Bragg plane parallel to the crystal's surface was  $\text{Si}(1,1,1) \pm 0.5^\circ$ , the  $\text{Si}(5,5,5)$  reflection from this crystal was used to reflect x-rays of 9.989 keV from the mercury  $L_{\alpha 1}$  spectral line [26]. This photon energy at (5,5,5) Bragg reflection corresponds a Bragg angle of  $81.7^\circ$ .

It is also important to again recognize that each crystal offers a limited energy range with which it can be used to produce HERFD results. For instance, while using the (5,5,5) reflection, the range of allowed energies is less than 400 eV due to the need to maintain a Bragg angle of over  $75^\circ$ , thus greatly limiting the number of edges that a given crystal/reflection can be used for. As such, a user ready HERFD end station requires a library of crystals with a variety of cuts in order to produce the highest quality result.

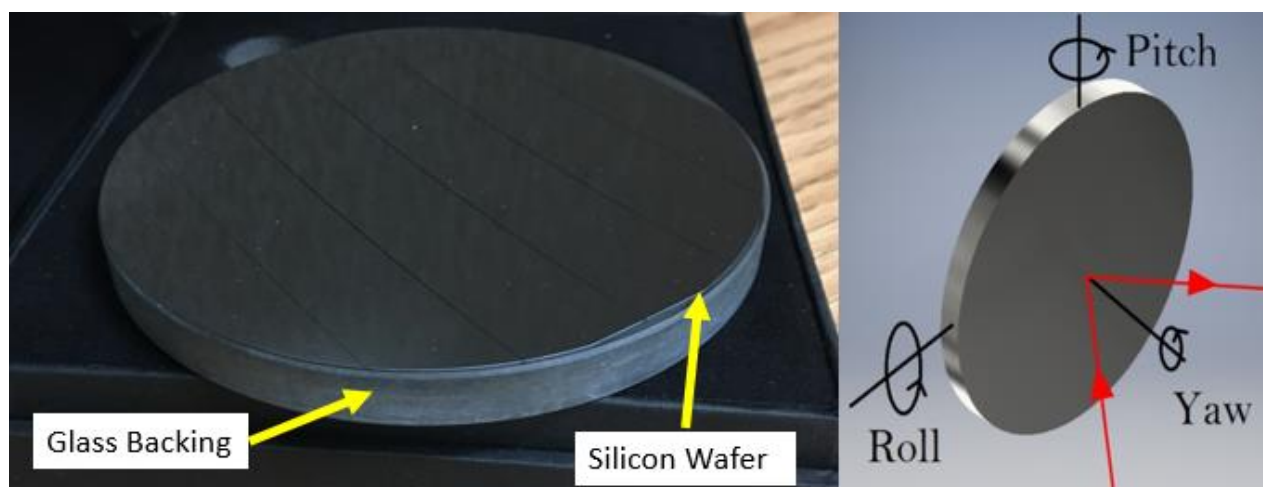


**Figure 3.2:** **Left** - An image of the Si(1,1,1) analyzer crystal that was used for this thesis investigation, on its surface the strip cut silicon wafer can be seen. In addition, the glass backing it is mounted on is visible, this is the portion of the analyzer that the mount will clamp onto. **Right** - A schematic of the analyzer crystal displaying the rotation axis that will be used for discussion in this thesis.

The crystal was placed in a tiered metal ring with levels such that its surface would be flush with the outside of the ring, a plastic screw through the ring was used to secure the crystal. This metal ring was then mounted onto a backing plate using two screws (Fig. 3.3), in the future this would allow for the crystal to easily be exchanged with another

without losing the established alignment. Below in Figure 3.3, a rendering of this mounting system can be seen side by side with an image of the crystal mounted in it.

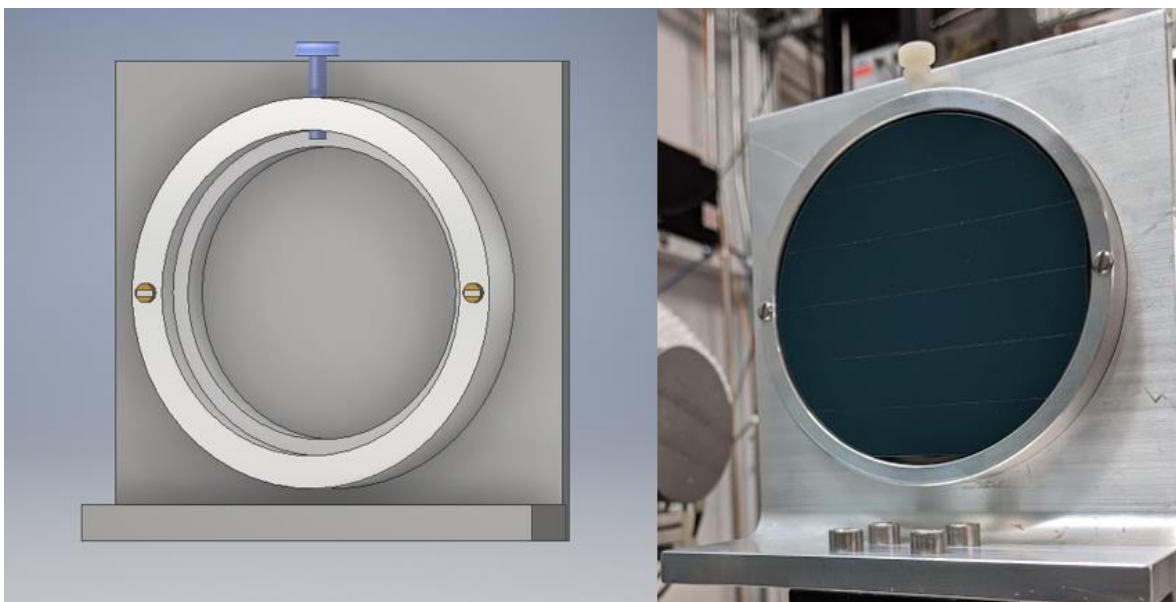


**Figure 3.3:** **Left** - A schematic diagram of the crystal mount that was manufactured for this project, the tiered ring that holds the crystal is shown mounted to the backing plate with two screws. **Right** – A photo displaying the crystal analyzer mounted in place.

### 3.2.2 Energy Resolving Detector

A 4-element Vortex silicon drift detector was selected from the HXMA equipment pool. This detector has an energy resolution of approximately 150 eV and as such allowed for background signals to be rejected acting as a wide band pass filter [27]. In addition, the ability to monitor all four elements allowed for a rough understanding of the dimension of the focused beam spot. Focusing the analyzed beam onto a single element ensured it was less than 1 cm in diameter, ideally it should be the same size as the beam spot on

the sample. Focusing onto a single element also provided a starting point to further aperture the analyzed beam prior to detection.

Ideally, future experiments will be run with a PILATUS3 area detector [28]. This allows for real time beam size monitoring and simplifies rejecting counts outside a selected region. However, ultimately a detector of this caliber wouldn't be required in an established HERFD system and something as simple as a photodiode could be used to collect the reflected fluorescent rays. Due to the crystal analyzer the signal to noise seen by any of these detectors isn't expected to be a concern.

The 4-element detector was mounted onto an adjustable platform with five degrees of freedom, the adjustments made using this platform and their use will be described in section 3.2.3.

### **3.2.3 Motor Controls and Moving on the Rowland Circle**

A major challenge when working with a HERFD system that has yet to be addressed is versatility and the ability to quickly adjust the Bragg angle. In the system constructed for this thesis these adjustments were made by a series of motion stages, some manual and some driven by two and five phase stepping motors. The mechanics within a stepping motor will not be addressed by this thesis and only the terminology that will be used is step size. Step size is simply the smallest possible adjustment the motor can make resulting in a set displacement (On the order of microns for the motors that were used).

The controls on the analyzer and detector stack will be described below, the coordinate system used for this discussion follows that seen above in Figure 3.1 and 3.2. The  $x$ -direction denotes movements parallel to the beam and the  $y$ -direction perpendicular to it in the storage ring plane, the  $z$ -direction relates to vertical adjustments (of which there should be minimal). Angular dimensions refer to roll as the crystal face being leaned forward or backwards (Fig.3.2), pitch as a rotation side to side (controlling the Bragg angle) and yaw as spinning about its center.

The basis of movement for the HERFD system was constructed to have a fixed location for the sample (as the beam should be incident to the same point on the sample for any Bragg angle) and have the analyzer and detector move with respect to it (while always residing on a Rowland circle) satisfying the Bragg condition of interest. As such the only adjustments made to the sample were in the  $z$ -direction ensuring it was at the same height as the incoming beam. Below the available adjustments for the detector and analyzer stacks are described.

**Analyzer Stack:** The crystal analyzer location and angle were controlled using five degrees of freedom, four controlled by stepping motors and one manually adjustable. The manual adjustment was for its  $z$ -coordinate using a lab jack the manual adjustment was adequate as no dynamic adjustments were required and it could be positioned using a laser level. The  $x$  and  $y$  coordinates were controlled using a two and five stepping motor stage respectively, as a smaller adjustment in  $y$  would result in a larger change in Bragg angle. The crystal had stepping motors stages to control its pitch and roll, this allowed for

minor scanning to ensure the crystal face was normal and tangent to the Rowland circle. Below in Figure 3.4 a schematic diagram of this stack can be seen for visualization purposes.

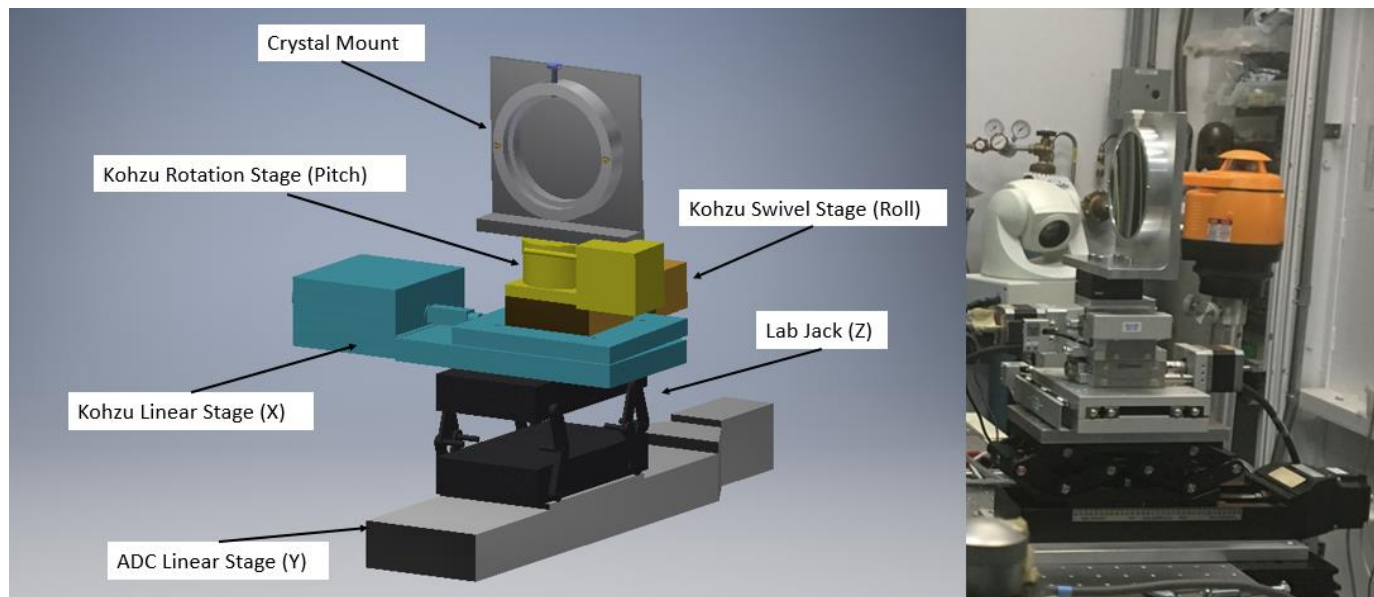


**Figure 3.4:** A schematic diagram and picture of the analyzer stack used for this experiment. Labeled in the schematic are the control stages used for positioning and scanning.

For the model number and step size of all stages and motors mentioned above see Appendix A.

**Detector Stack:** Comprised of three manual and one motorized stage the detector stack is equipped to completed standard HERFD scans and mapping. The manual stages were for pitch,  $x$  and  $z$  (Fig. 3.5) as they do not require adjustments during mapping; pitch was controlled by a 1-circle goniometer,  $x$  by a manual linear motion stage and  $z$  by a lab jack.

The motorized stage was controlled by a stepping motor which adjusted the detectors  $x$  coordinate, as explained in section 2.4.2 this is the only adjust required of the detector to complete a RIXS energy map. Below in Figure 3.5 a schematic diagram of this stack can be seen for visualization purposes.

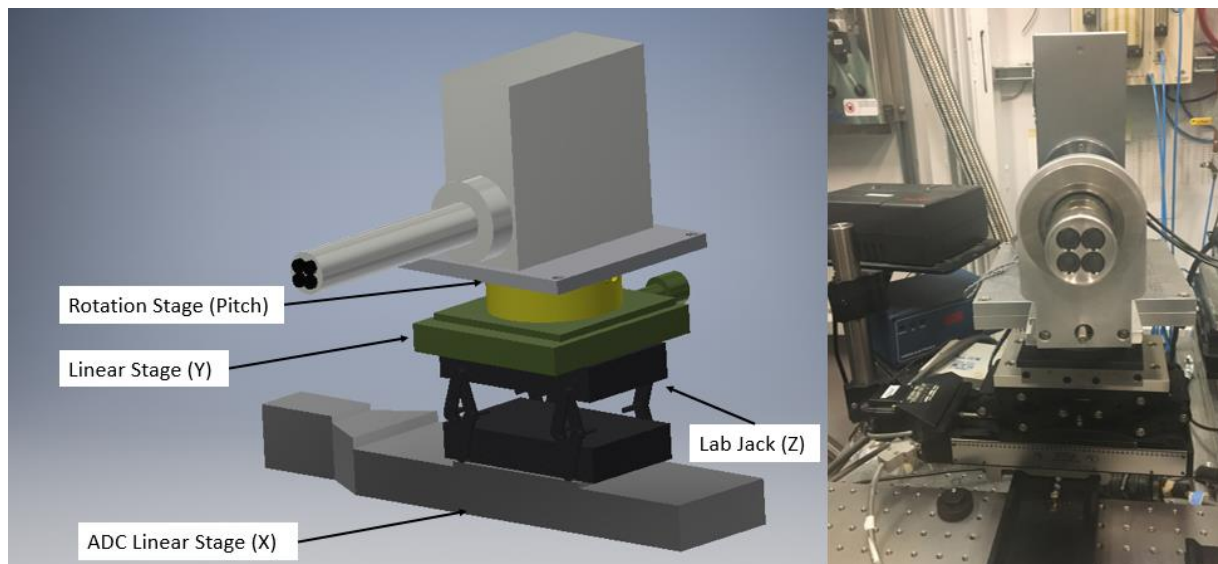


**Figure 3.5:** A schematic diagram and picture of the detector stack used for this experiment. Labeled in the schematic are the control stages used for positioning and scanning.

For the model number and step size of all stages and motors mentioned above see Appendix A.

The sample and detector stacks were mounted onto sliding clamps that were locked onto optical rails fixed to the breadboard. The analyzer stack was mounted directly onto the breadboard. The fully assembled system can be seen below in Figure 3.6. In addition to the components that have been addressed thus far in this section Figure 3.6 also

displays the addition shielding used in this experiment. The sample was placed in a 3-d printed two walled box with lead tape covering it, an addition piece of lead covered sheet metal was added to the downstream side of this box. All this shielding was to ensure that any beam that passed through the sample would not reach the detector which had to be positioned directly downstream in the beam path to satisfy Johann geometry.

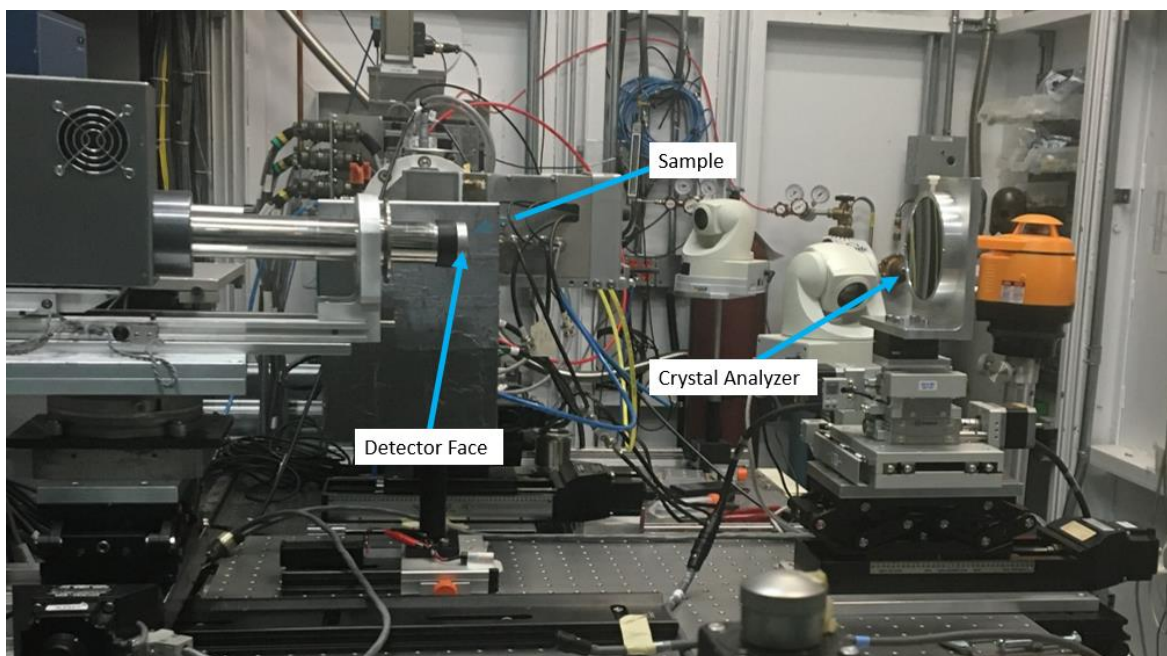


**Figure 3.6.a:** The experimental HERFD arrangement viewed from downstream from the sample point. The sample is behind lead shielding and thus is not visible. However, both the detector and analyzer stacks can be clearly viewed following the schematics shown in Figure 3.4, 3.5.

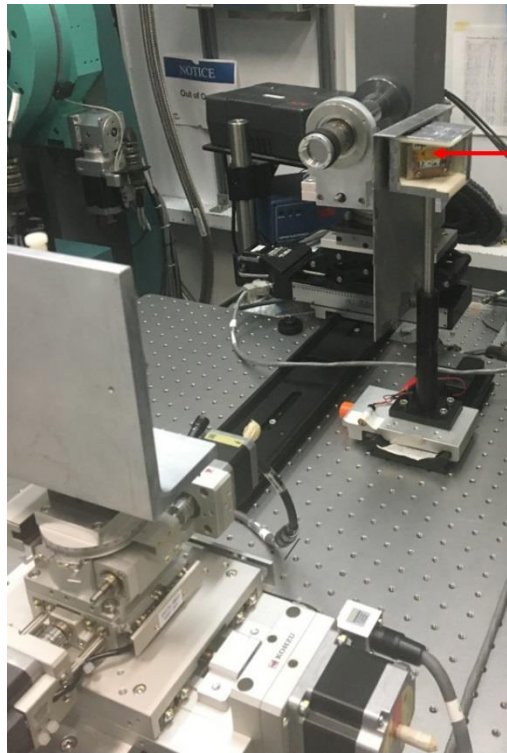


**Figure 3.6.b:** The experimental HERFD arrangement viewed perpendicular to the beam. Here the sample can be clearly viewed as well as the crystal back and detector. This figure also shows the beryllium window over the four-element detector to protect the detector surface.

### 3.3 Sample Selection and Preparation

Due to the unknown nature and yield of the HERFD system going into this experiment a range of samples with various concentrations were made. Ideally the lowest concentration would yield the best results in terms of spectral fidelity; however, an adequately strong signal is paramount to spectra collection efficiency [29]. Loss in signal in the HERFD system can be attributed to losses on various interfaces and due to travel through air (approximately 1 m of travel post sample).

The samples were prepared following the same procedure as standard fluorescence experiments [29]. First, the raw sample was ground using a mortar and pestle to be fine grains. The ground materials were then sieved through a set of sieves with decreasing hole size, the smallest of which being 53 microns in diameter. Only the ground sample which was able to pass through this final sieve was used thus ensuring a minimal particle size to avoid any self-absorption. The ground and sieved sample was then diluted with boron nitride, the result of the dilutions were samples with a concentration by weight ranging from 0.1% to 3%. To ensure the diluted samples were homogenous the mixture was loaded into a grinding jar with plastic beads and placed in a ball mill. Post milling the sample was transferred into an anvil where it would be pressed into a pellet under approximately 8 tons of pressure for 180 sec. Finally, the pressed pellet would be set and taped onto a plastic sample slide using Kapton tape (thickness 71  $\mu m$ ), this arrangement can be seen in Figure 3.7.

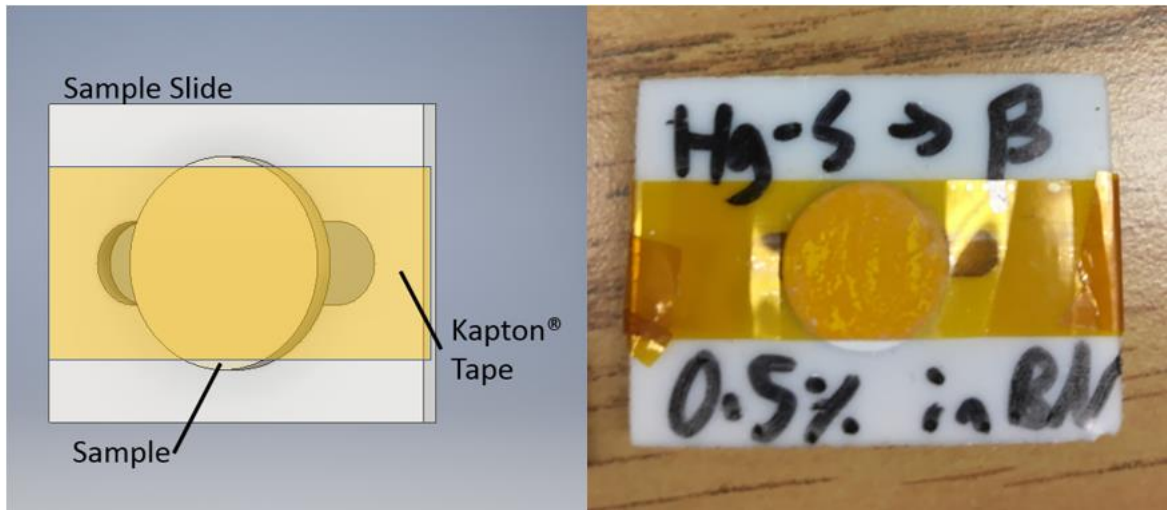


**Figure 3.7:** A schematic diagram and image of the prepared sample mounted on a sample slide and secured using Kapton® tape.

Two sample materials were prepared in this manner; cinnabar mercury sulfide ( $\text{HgS-}\alpha$ ) and metacinnabar mercury sulfide ( $\text{HgS-}\beta$ ). These are two of the three trimorphic states of mercury sulfide, hypercinnabar was not included in this investigation due to its scarce nature. The two states of HgS have a vastly different structure as can be seen in Figure 3.8, cinnabar having a trigonal trapezohedral crystal structure and metacinnabar having a zinc-blende crystal structure [30]. The anticipated spectral differences from these compounds will be described in section 4.2.

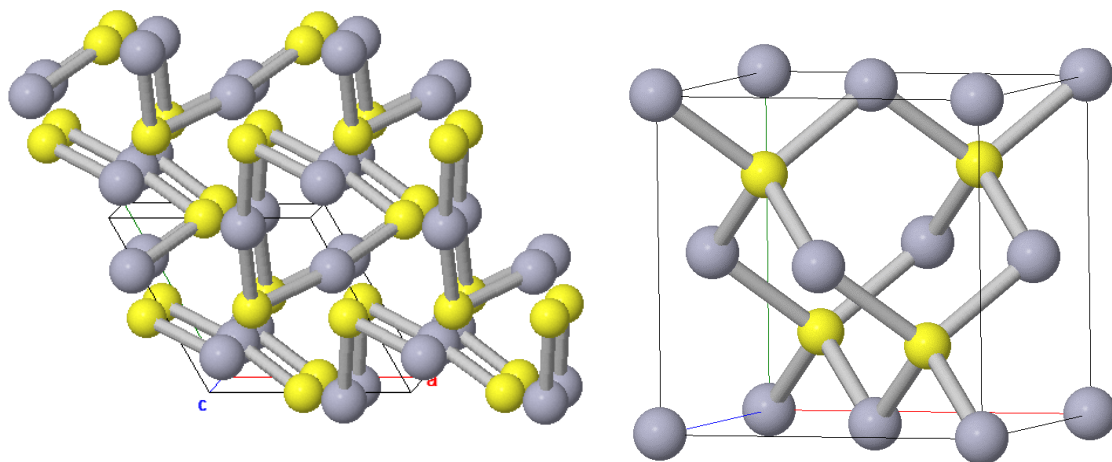


**Figure 3.8:** The sample structures of the compounds of interest to this thesis. Mercury atoms are displayed in grey and sulfur atoms in yellow. Left: Cinnabar (HgS- $\alpha$ ) the more open of the two structures displaying trigonal trapezohedral symmetry. Right: Metacinnabar the more closed structure of the two displaying zinc-blende structure. [30]

## 4 Experimentation and Data Analysis

### 4.1 Intended Scanning Routine

The first objective when beginning a HERFD experiment is to align all optical components onto the desired Rowland circle. As the system being used in this experiment is not permanently mounted this task is arduous as all attained results are predicated by the quality of the initial optical alignment. As such, this alignment consumed a large amount of beamtime.

To begin the assembly the moveable breadboard was mounted onto the experimental hutch optical table (HXMA-BL XAFS station in SOE) using its existing optical rails. Once the table was locked in place the stacks (previously outlined in Section 3.2.3) were assembled and mounted in their respective locations. These locations were coarsely determined by measurements done by hand ensuring the analyzer crystal, sample and detector were within a half inch of their desired  $x$  and  $y$  locations. A laser level was then used to adjust the stacks  $z$  coordinate to be level with the beam and in plane with the storage ring. The sample shielding was then attached to ensure the safety of the 4-element detector. This shielding was made to be several times redundant as the detector was directly in the beam path and is naturally very susceptible to being oversaturated potentially damaging it and at the very least consuming valuable time while excess charge dissipates.

With the optical components roughly positioned and the required shielding in place the system was ready to have the x-ray beam introduced. Prior to its introduction the

beam had to be calibrated and trimmed. To begin the monochromator crystal selection was moved to the Si(1,1,1) crystals, the center of JJ x-ray slits [24] were scanned allowing the most photon dense 1 mm by 1 mm beam to pass. The optical arrangement used for the calibration scan can be seen below in Figure 4.1. As displayed, a copper sample was placed past the first ionization chamber as the copper k-edge was to be scanned using the first ionization chamber for ( $I_0$ ) and a Lytle chamber (placed perpendicular to the sample point) to measure fluorescence intensity ( $I_f$ ).

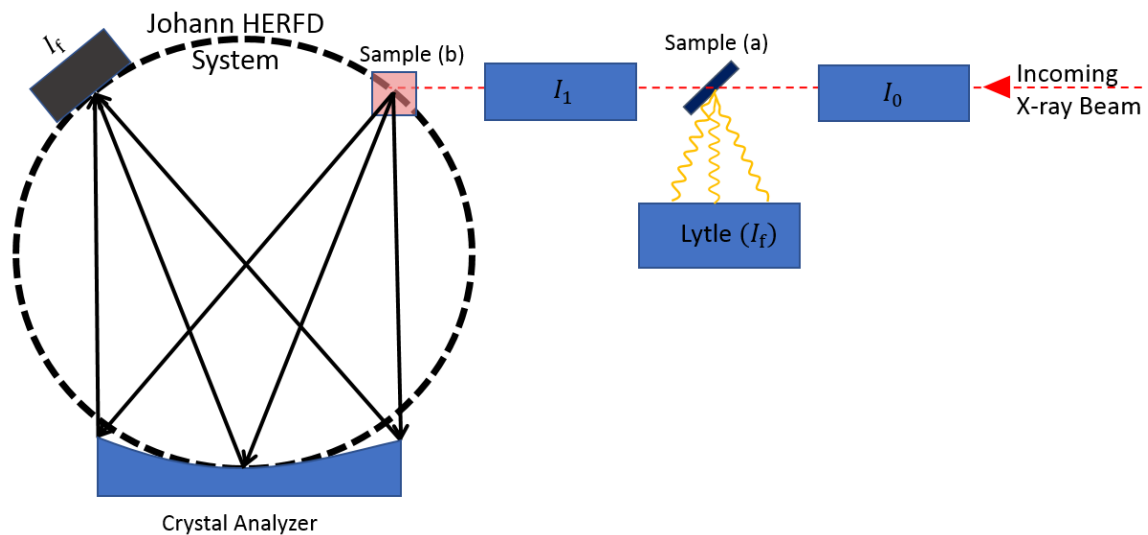


**Figure 4.1:** A schematic diagram of the optical components on the experimental optical hutch optical table. Displayed is the system used for calibration and conventional scans composed of ionization chambers and a Lytle chamber. In addition, the HERFD position is shown positioned downstream from the second ionization chamber. While collecting the conventional spectra the sample will be in location (a) and to collect HERFD spectra the sample will be moved to location (b). (Components and distances in this figure are not to scale as it is intended to present the orientation of the optical components)

Prior to this scan the monochromator was detuned to 50% for rejecting harmonics of the fundamental wavelength. The dark current seen in the ionization and Lytle chambers was recorded and subtracted. (This process of detuning, scanning the JJ x-ray slits and subtracting the dark current was also completed after each storage ring current injection.) With the x-ray slits aligned, detuning and dark current subtraction completed the copper calibration scan was run and the beam was prepared to begin experimentation. It should be noted that the energy resolution of the Si(1,1,1) monochromator is on the order of  $\frac{\Delta E}{E} \sim 10^{-4}$  and as such should be approximately 1.2 – 1.5 eV for the energy range of interest to this thesis. This resolution is determined using the Darwin width of a flat Si(1,1,1) crystal at a given energy and relating it to a level of energy uncertainty [31].

After completing the calibration, the copper sample was removed and replaced with a 1% HgS- $\alpha$  sample and the JJ x-ray slits were adjusted to be 1 mm (vertical) by 3 mm (horizontal). Using this arrangement conventional fluorescence results were collected to be used as a comparison with the HERFD results that would hopefully be attained later in the experiment. The conventional scans using the Lytle chamber were also collected for the 1% HgS- $\beta$  sample. The conventional spectra for both samples can be seen below in Figure 4.2.

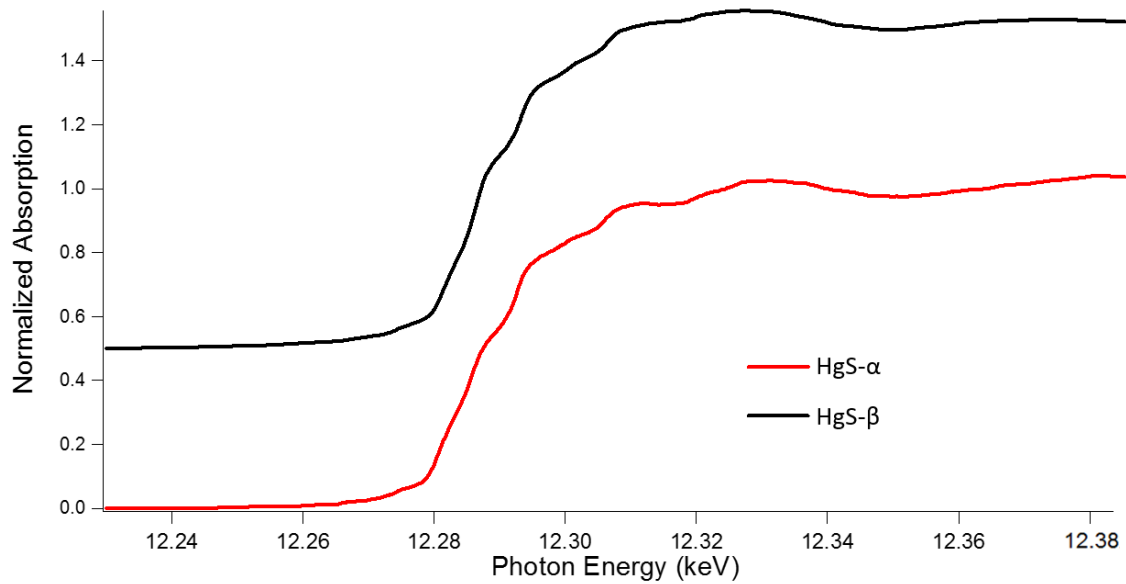


**Figure 4.2:** Displayed are the resulting spectra from conventional fluorescence detection for cinnabar (HgS- $\alpha$ ) and metacinnabar (HgS- $\beta$ )

With the conventional scans completed the focus was moved back to HERFD alignment. The next step in this process was to ensure the beam was incident to the HERFD sample stand near its center, this was done using a piece of x-ray sensitive photograph paper on the samples surface. This step isn't abundantly necessary as the sample is large in comparison to the beam however it is a minimal time investment for assurance that the beam is incident to the sample and not hitting other metal components in the sample holder.

At this point it is understood that the HERFD optical components are only roughly aligned so a high-resolution scan is not yet expected. However, taking a spectrum of HgS- $\alpha$  with the 4-element detector allowed for the energy window of interest to be selected. In

addition, this will provide a starting point for the further refinements to come and be usable as a comparison between using the analyzer crystal to satisfy the desired Bragg condition vs. working as a simple mirror. This scan will be displayed in Figure 4.3 alongside the spectra taken as spectral resolution was improved via more precise positioning. It is important to note that with this alignment the count rate seen by a single element of the detector was on the order of a thousand counts, a number that should greatly increase with proper positioning/focusing.

The first step in improving the resolution of the system was to ensure the analyzer crystal was correctly positioned on the Rowland circle. To do this a constant incident beam energy of 17 keV was held while various motors were scanned in pairs while monitoring the photon counts seen by the various elements in the detector. The selection of incident energy was based on the intention of exciting mercury L-edge electrons from the sample into continuum and avoiding any near edge features. In this energy regime the larger the area of the crystal analyzer which meets the Bragg condition of the  $L_{\alpha 1}$  photons the higher the count rate the detector will see. It is also important to recall that in the ideal scenario the crystal analyzer will focus the fluorescence emission to a point on the detector that is the same size as the beam spot on the sample and as such all focusing measures were only concerned with counts on a single element of the detector.

The initial scans that were used to optimize the position of the crystal analyzer involved moving its  $x$  (along the beam path) and  $y$  (transverse to the beam path) position and monitoring the detector counting rate. These scans covered over a half inch in each

direction ensuring that the scanned area covered any potential error in the alignment that was completed by hand. The scans started with a coarse step size that was continually decreased as the region with the highest count rate was found.

This scanning process was then repeated for other sets of motors. The sets that were scanned together were the crystal analyzer's pitch and roll, the detector's  $x$  position independently, the detector and analyzer  $x$  positions and finally the analyzer's  $y$  position with the detector's  $x$  position. The resulting spectra after these scans be seen in Figure 4.3 where it is clear that the spectral resolution of the system had improved. This is most apparent in the pre-edge feature of HgS- $\alpha$  where the conventional and misaligned scan don't display a peak with any definition on the rising edge in contrast the spectra approaching a HERFD scan shows a peak with low fluorescence intensity difference but is well defined.

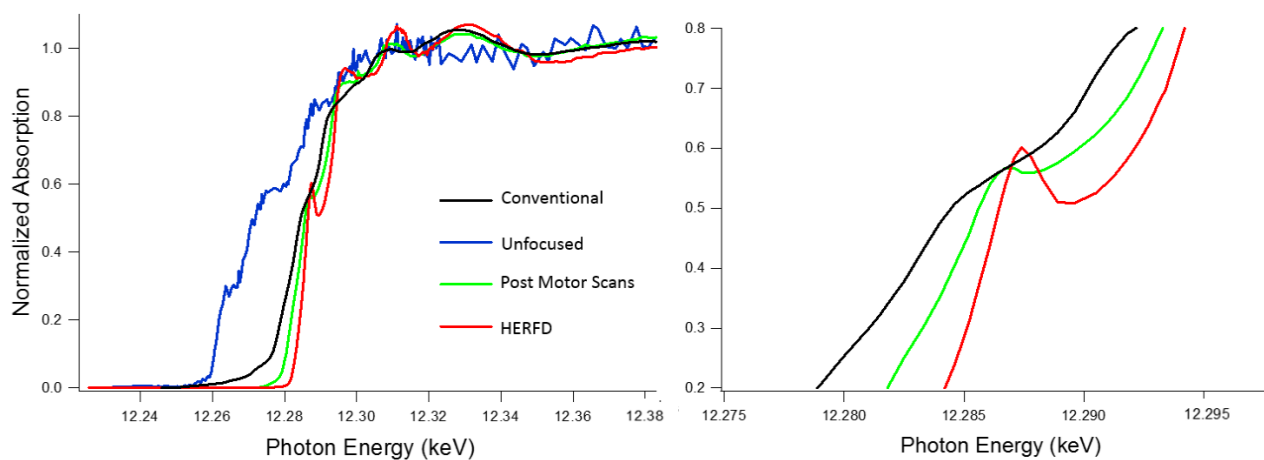


**Figure 4.3:** Displayed are the resulting spectra from the conventional fluorescence detection, the unfocused HERFD arrangement, the HERFD arrangement after motor scans and the final HERFD scans.

A detail that may cause concern when viewing these results and those that will be featured further in this text is the apparent shift in edge energy. This shift is a by-product of the partial fluorescence yield that the HERFD system is taking. Depending on the emitted energy that is being reflected by the analyzer, the edge may appear to be at a higher or lower energy than it truly is, the cause of this can be seen below in Figure 4.4. Simply put, this shift is a product of crossing the resonance feature with an analyzer energy that does not pass through the resonance's maxima. However, even with this in mind the features and spectral shape seen in the spectra collected with the unfocused system are not fully understood. This further demonstrates the need for RIXS mapping for a complete understanding of an unknown sample system. For further details see Glatzel et. al [4].

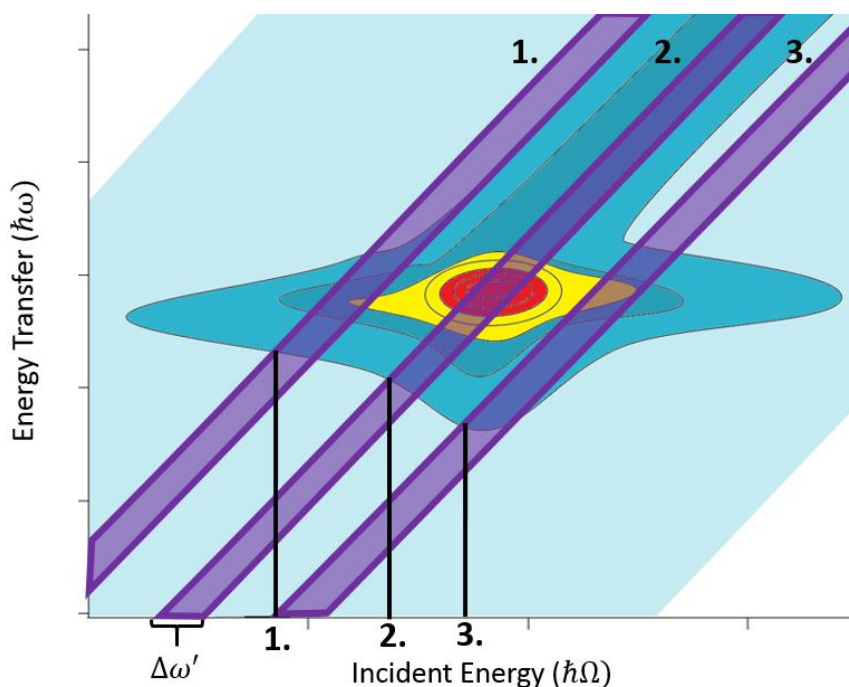


**Figure 4.4:** Shown on this RIXS map is the cause of the apparent edge shift seen when varying the analyzed energy. Here the rising edge will appear at a progressively higher energy as one moves from analyzer energy 1 to 2 to 3.

The next improvement to be made after completing the motor scans was to introduce an aperture to the face of the detector. This allowed for a smaller area of reflected fluorescence photons to be accepted by the detector. For this experiment the aperture was rigid and made from lead tape; however, later in development the HERFD system would utilize a set of motorized Huber [32] slits to dynamically scan over the detectors surface. These dynamic scans would allow more information on the shape and photon distribution of the reflected fluorescence. However, even the addition of the rigid lead tape aperture of 1 mm x 3 mm in conjunction with scanning the detectors  $x$

coordinate allowed for dramatic improvement. The final resulting spectra can be seen in Figure 4.3 and more details pertaining to it are given in Section 4.2.

## **4.2 Comparison to Published Results**

This section will discuss the results produced after the previously mentioned motor scans were completed and the detector was apertured. The intent is to clearly display the increased spectral resolution, discuss the atomic structural origin differences that lead to the spectral differences among the samples tested and compare the HXMA results to those from a published and active HERFD endstations. To begin, the results of this thesis experimentation are shown below in Figure 4.5 featuring the spectra for both HgS- $\alpha$  and HgS- $\beta$  collected using a HERFD arrangement and using conventional fluorescence detection. The spectral improvement is abundantly clear and shows promise for the use of this technique. The other detail that should be addressed at this point is the count rate after the focusing had been completed. Prior to the motor scans and aperture, a single element on the Vortex™ detector was seeing on the order of 1000 counts/sec (integrated over the region of interest surrounding the Hg L $\alpha$  line). After focusing and even with the aperture present the count rate in the focused element was on the order of 10,000 counts/sec. This shows a dramatic count rate increase when the crystal analyzer is focusing at an appropriate Bragg angle.

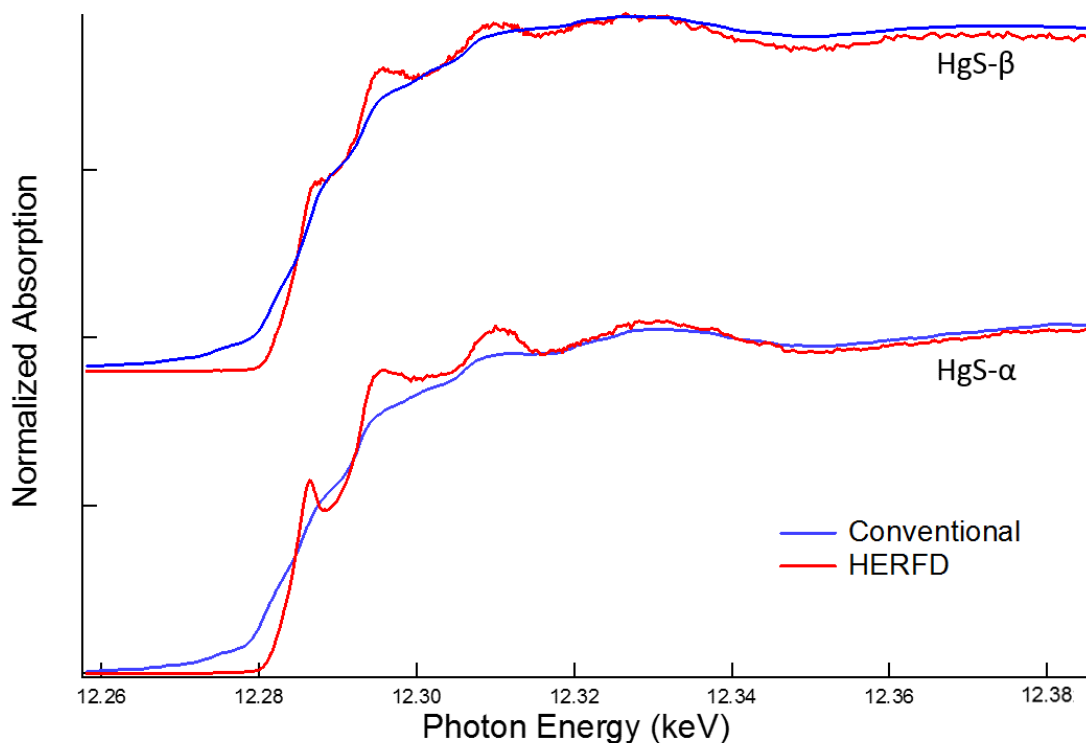


**Figure 4.5:** The final results of the HERFD data collection working with both cinnabar (HgS- $\alpha$ ) and metacinnabar (HgS- $\beta$ ) plotted with the conventional results.

Prior to discussing the spectral improvements seen between the HERFD and conventional scan, it is important to discuss the differences between the alpha and beta phase of mercury sulfide. While the spectral differences are rather minimal in the conventional spectra there is significant deviation with the increased resolution. These differences are entirely based on the atomic structure of the two compounds as the chemical make-up is identical between the samples. Metacinnabar has a zinc-blende structure meaning it is tetrahedral with the mercury atom coordinated to four sulfur atoms.

In contrast, cinnabar has a trigonal trapezohedron structure, which can be visualized as triangular spirals of a mercury atoms coordinated to two sulfur atoms. This structure has hollow tubes down the spirals leading to empty space. (See Figure 3.8)

In the XANES region both samples show four peak features with varying degrees of sharpness. The spectral improvements can be seen on each of the peaks and for both samples with the most dramatic changes being seen in cinnabar (HgS- $\alpha$ ) especially on the pre-edge peak ( $\sim 12,286$  eV), this peak will be used as a comparison tool when comparing the HXMA results to other HERFD-XAS systems below. Another note to be made when comparing the HERFD result to the conventional spectra is the minimized background signal, the analyzer removes any background signal leaving counts on the order of 10-20 compared to a signal strength of 10,000. In contrast, one will notice a higher level of noise in the HERFD scans, this stems from using a significantly weaker signal with limited counting statistics due to only allowing a narrow energy band to pass to the detector.

The results shown above can be compared to the results produced by O. Proux et al. at the European Synchrotron Radiation Facility (ESRF) at beamline BM30B and BM16 (where there is an active HERFD endstation) [2]. This HERFD-XAS arrangement was also constructed using a Johann crystal arrangement, however it used a Rowland circle with a 1 m radius (double that which was constructed at HXMA). The published results of can be seen below in Figure 4.6.

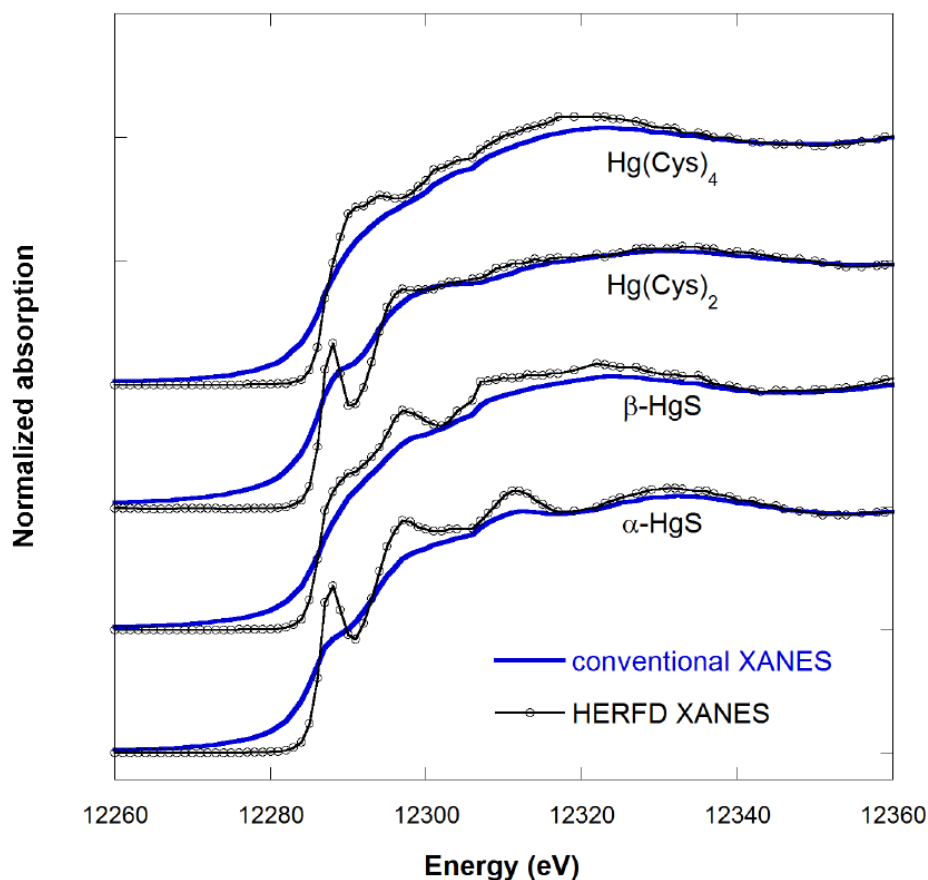


**Figure 4.6:** Spectra from the mercury  $L_{III}$  edge produced at ESRF on beamline BM16 showing conventional and HERFD results for cinnabar ( $HgS-\alpha$ ) and metacinnabar ( $HgS-\beta$ ) Source: Proux et. al. 2017, figure 3 (p. 13). [22] Reprinted with permission of John Wiley & Sons. Inc. [2]

The resolution seen in Figure 4.6 is greater than that shown in the HXMA HERFD results of Figure 4.5. This difference can be most notably seen in the pre-edge feature of  $HgS-\alpha$  where the HXMA peak to valley ratio is approximately 0.58:0.48 and the BM30B/BM16 peak to valley ratio is 0.67:0.48, highlighting the higher level of spectral sharpness [2]. There are a few factors leading to this, the first comes from the increased Rowland circle radius (1 m) which inherently improves the resolution following:

$$\frac{\Delta E}{E} \propto \frac{\Delta R}{R} \quad (11)$$

here  $\Delta R$  is the radius of the detector aperture,  $R$  is the radius of the Rowland circle,  $E$  is the analyzed energy and  $\Delta E$  is the energy resolution. Clearly increasing the radius of the Rowland circle will have a positive result on the resolution of the system. In addition, the BM30B/BM16 arrangement is built using five crystal analyzers and is now a fully operational system which accepts user applications; therefore, it is believed to be in its optimized alignment status [2]. Thirdly, there are some additional details (e.g. the sizes of the various beam limiting aperture) that are not yet available from the literature that could also lead to additional enhancement on the energy resolution if the acquisition time is less of a concern. Further to this point the test system used at HXMA was operated in a relatively time limited environment for both assembly, calibration and testing and while the results shown above are promising they may not have yet reached the best attainable results by the current system. As an outside user group collaborating with CLS significant travel was require and HXMA beamtime had be allocated to other tests as outlined in Section 4.3 and 4.4.

Moving forward from this initial feasibility study HXMA should be able to compete and hold some advantages when comparing the beamlines. A major boon HXMA has is the difference in x-ray source with HXMA using a wiggler and BM30B and BM16 both using a bending magnet. This means that HXMA has a brilliance on the order of 60x higher than the bending magnet beamlines. This gap is somewhat mediated using a five-

crystal arrangement at BM16. However, HXMA would also ultimately adopt a multi-crystal system and would be capable of providing a faster acquisition time and allow for a higher level of photon rejection. The major feature at the bending magnet beamlines that may not be feasible at HXMA is the size of the Rowland circle. The HXMA secondary optical hutch is already constructed and used for other XAFS experiments and space is somewhat limited for the dedicated HERFD endstation, leading to a limitation on maximum size of the Rowland circle.

In addition to the results produced at ESRF, there have been developments working with HERFD at the Advanced Photon Source (APS) in the USA. There is a collaborative development project through the CLS @ APS initiative with Dr. Zou Finrock being the correspondent. This development is moving forward to a dedicated endstation and has shown some remarkable results including spectra of cinnabar mercury sulfide, this result can be seen below in Figure 4.7. Clearly this result has increased spectral sharpening over both the HXMA and the ESRF results. One major root cause for this and a barrier that HXMA cannot overcome in its current configuration is the photon source used. The work at APS has been done using a undulator beamline (sourced by APS Undulator-A) with a brilliance about one hundred times that of the HXMA wiggler. This in turn means the same data acquisition would take far less time and a larger portion of analyzed/reflected signal could be rejected allowing for smaller apertures. This will further necessitate a multi-crystal system be used at HXMA to regain counting efficiency by capturing a larger solid angle.

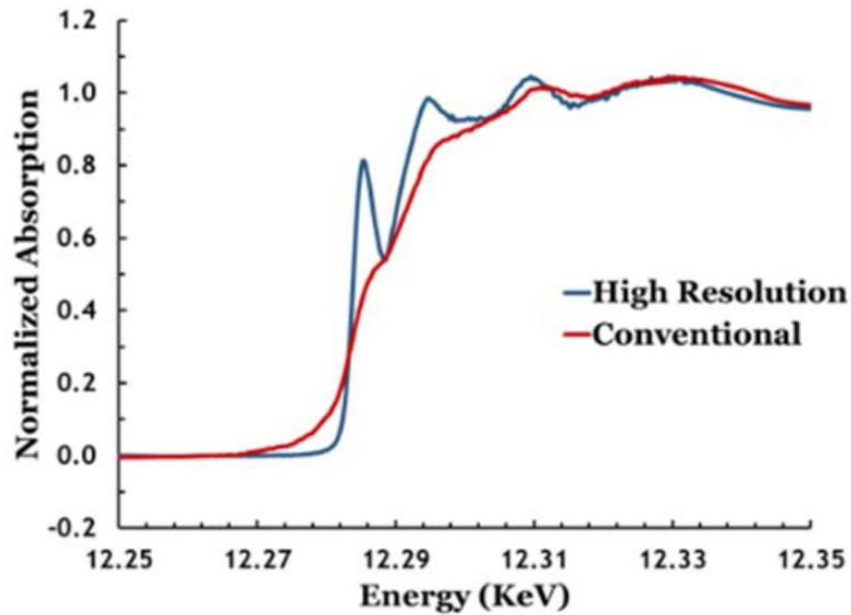


**Figure 4.7:** The spectra collected at APS for cinnabar (HgS- $\alpha$ ) collected using both conventional fluorescence detection and HERFD .

With all results above considered, the outlook of this feasibility study is quite promising, and the improved spectral resolution is more than apparent. There are still a couple investigations to be completed before beginning work on the permanent HERFD endstation as outlined in Sections 4.3 and 5.1. A dedicated HERFD-XAS endstation at HXMA seems both viable and promising, its inclusion would introduce a new XAS technique to Canada and lead to high quality scientific results.

### **4.3 Intended Procedures for RIXS Mapping**

Thus far in this feasibility study the largest missing feature is an energy map generated by the HERFD system. This would logically be the next investigation and would require no alteration to the existing system, the main goals of mapping would be to provide an optimized line-scan path and an evaluation of the system energy resolution; also this would allow our results being comparable with those obtained in other HERFD facilities. In addition, it would begin the development of an automated routine which would become a tool for any HXMA user to create an accurate map while only providing minimal parameters.

Optimization of this mapping process will become the focal point and capstone of the remainder of this feasibility study. If this system can complete mapping and HERFD scans of two to three different samples within the standard 6 shifts (48 hours) of beamtime it can be added to the list of operable equipment. In addition, the production of an energy map is expected to improve the quality and reproducibility of the HERFD scans. This improvement stems from ensuring the analyzer energy is properly tuned to cross the maxima of the fluorescence line.

The intended mapping procedure roughly follows the procedure outlined in Section 2.4.2 with a more detailed and system specific description provided below. To reiterate the RIXS maps produced are a three-dimensional map with the dimension of energy transfer on the y-axis, incident/photon energy on the x-axis and signal intensity providing the topography. These maps are populated by a set of individually collect line scans

associated with a set analyzer energy and a scanned range of photon energy (a XANES scan at a given analyzer energy). Each line will lay diagonally across the RIXS map and through collecting these scans for many analyzer energies the map will become populated. In a known sample system this would allow for a compact RIXS map with dimensions on the order of 20 eV by 20 eV. When working with an unknown system one may wish to collect a larger and more sparingly populated map to ensure they have encompassed all features before starting the time intensive finely spaced mapping. These maps being a combination of many individual scans (XANES scans at varying analyzer Bragg angles) creates the need for a program that will stitch them together and display them with minimal hassle, this type of program won't be addressed by this thesis but is still invaluable when moving towards a user operated system.

The motion stages in play to complete RIXS mapping using the current arrangement (which is subject to change if the Rowland circle is moved to be vertically orientated as outlined in Section 4.4) are the analyzers  $x$  (Kohzu -XA16A-R202) and  $y$  (AVS - DS310-100) stages as well as the detectors  $x$  (AVS - DS310-100) stage (Figure 3.4, 3.5). The distance that each of these stages need to move to adjust to a new fluorescence photon energy is dependent on the Bragg angle setting of interest (as the analyzer Bragg angle setting increase the smaller the  $y$  translation required and the larger the  $x$  translations required). To adjust the analyzed energy one electron volt from 9.988 keV the detector  $x$  stage would move 0.6982 mm /  $\sim$ 140 steps, the analyzer  $x$  stage would move 0.3491 mm /  $\sim$ 70 steps and the analyzer  $y$  stage would move 0.0996 mm /  $\sim$ 25 steps. The position that each of the optical components is required to be is governed by the equations

found below, where the sample location is noted as  $(x, y) = (0,0)$ ,  $\theta$  is the analyzer Bragg angle given in degrees and  $x$  and  $y$  are in mm. (See Figure 4.8)

$$\text{Analyzer } x: x(\theta) = \frac{500}{\sec^2(90-\theta)} \cdot \tan(90 - \theta) \quad (12)$$

$$\text{Analyzer } y: y(\theta) = \frac{500}{\sec^2(90-\theta)} \quad (13)$$

$$\text{Detector } x: x(\theta) = \frac{1000}{\sec^2(90-\theta)} \cdot \tan(90 - \theta) \quad (14)$$

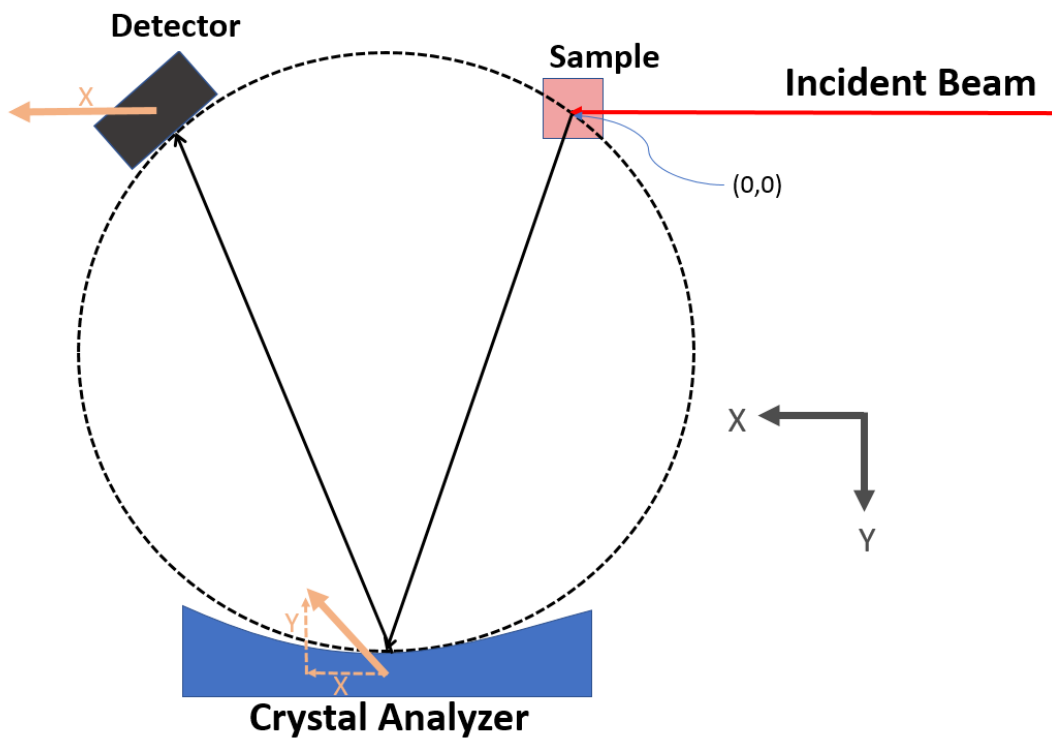


**Figure 4.8:** A schematic diagram of the movements undergone to move to a higher analyzed energy with the coordinate system imposed to follow the test system used at HXMA.

In addition, it is relevant to discuss stepping motor backlash. Backlash stems from a change in direction in conjunction with the gap in the gear teeth introducing a potential positioning error or inconsistency. To combat backlash the mapping routine should only have each motor travelling in a single direction for its entirety (including correction overrun).

Mapping could be completed via manual adjustments of each motor following the above equations. However, a permanent system would require a routine to have the system change the Bragg angle resulting in a small change in analyzed energy, scan and repeat. These changes in analyzer energy should be uniform and thus follow:

$$\theta' = \sin^{-1}\left(\frac{nhc}{2d(E + \Delta E)}\right). \quad (15)$$

Where  $d$  is the interplanar distance of the analyzer crystal,  $n$  is the order of the reflection being used,  $E$  is the current analyzer energy and  $\Delta E$  is the desired shift in energy. This new Bragg angle can then be used in conjunction with the position equations above to determine the locations for the next scan. This process can be completed ad nauseum until the map is adequately populated.

#### **4.4 Testing in Vertical Rowland Circle Configuration**

The final test that was completed during the work encompassed by this thesis was to test the viability of using a system based on a vertical Rowland circle. There are a few reasons a vertical system is more desirable. The first reason to move vertical is the natural

beam profile produced by a wiggler source as there is a rather large disparity in terms of vertical and horizontal angular spread of the beam [12]. HXMA's wiggler yields a beam that has minimal vertical dispersion and more significant horizontal dispersion. As such, the beam is already compressed in the vertical dimension and minimal flux loss will come from introducing an aperture in this dimension when compared to using the same aperture in the horizontal dimension. The second being space limitations and ease of access to the equipment. The geometry of the secondary optical hutch is simply more suited to have a vertical arrangement as the hutch is taller than it is wide.

The tests done within this thesis with a vertical Rowland circle were rather minimal and should simply be viewed as a test to whether increased spectral resolution can be easily attained using the analyzer crystal previously outlined. The same motion stages were used as in the horizontal system, however with this new arrangement the lack of motorized control on the  $z$  stages eliminated the ability to collect RIXS maps and conduct on possible focusing motor scans. Due to the motor scans being limited a lesser result to that seen in the horizontal system was expected. Seen below in Figure 4.9 is an image of the experimental arrangement used to collect the vertical Rowland circle data.

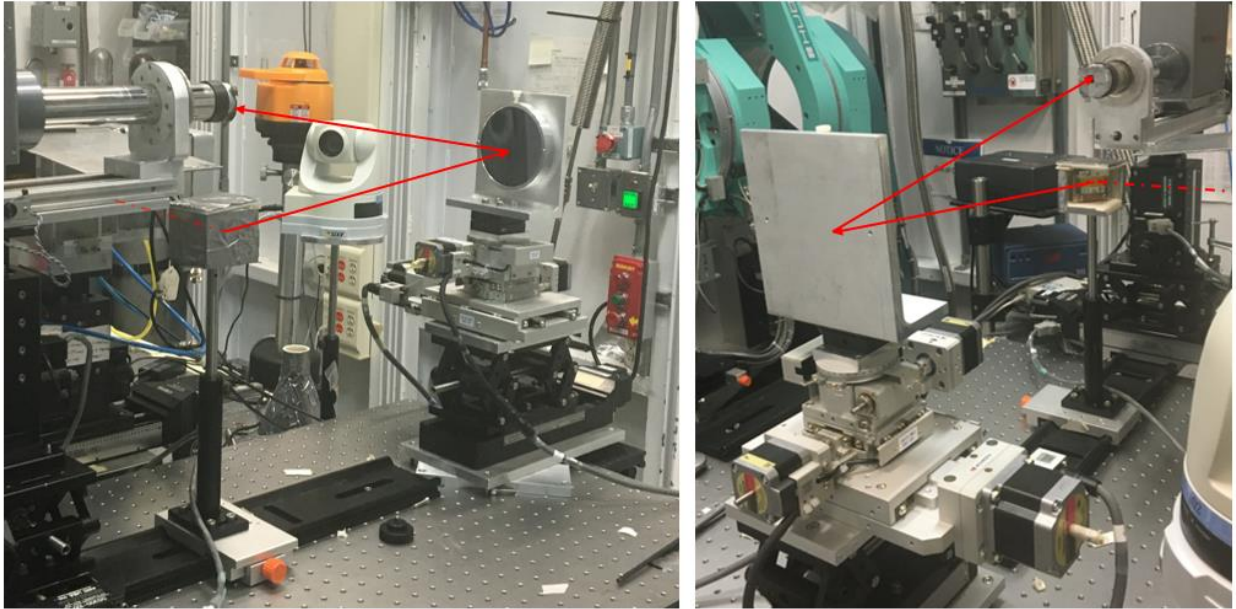


**Figure 4.9:** The experimental set-up used for vertical Rowland circle testing. **Left:** The downstream perspective showing the beam path and reflect fluorescence path. **Right:** The perspective perpendicular to the beam path showing the same paths as on the left.

The alignment procedure was similar to what was done for the horizontal Rowland circle. For each optical component the  $z$  coordinate was set using a laser level and the  $x$  and  $y$  were set roughly in position by hand. Following this, positioning via motor scans was completed. Both the detector and analyzer  $x$  positions were scanned to ensure they were aligned with the sample. The analyzer  $y$  position was scanned with its roll, followed by its  $x$  position with its pitch; in addition, pitch and roll were also scanned together to test the impact. The resulting spectra after these scans can be seen below in Figure 4.10.

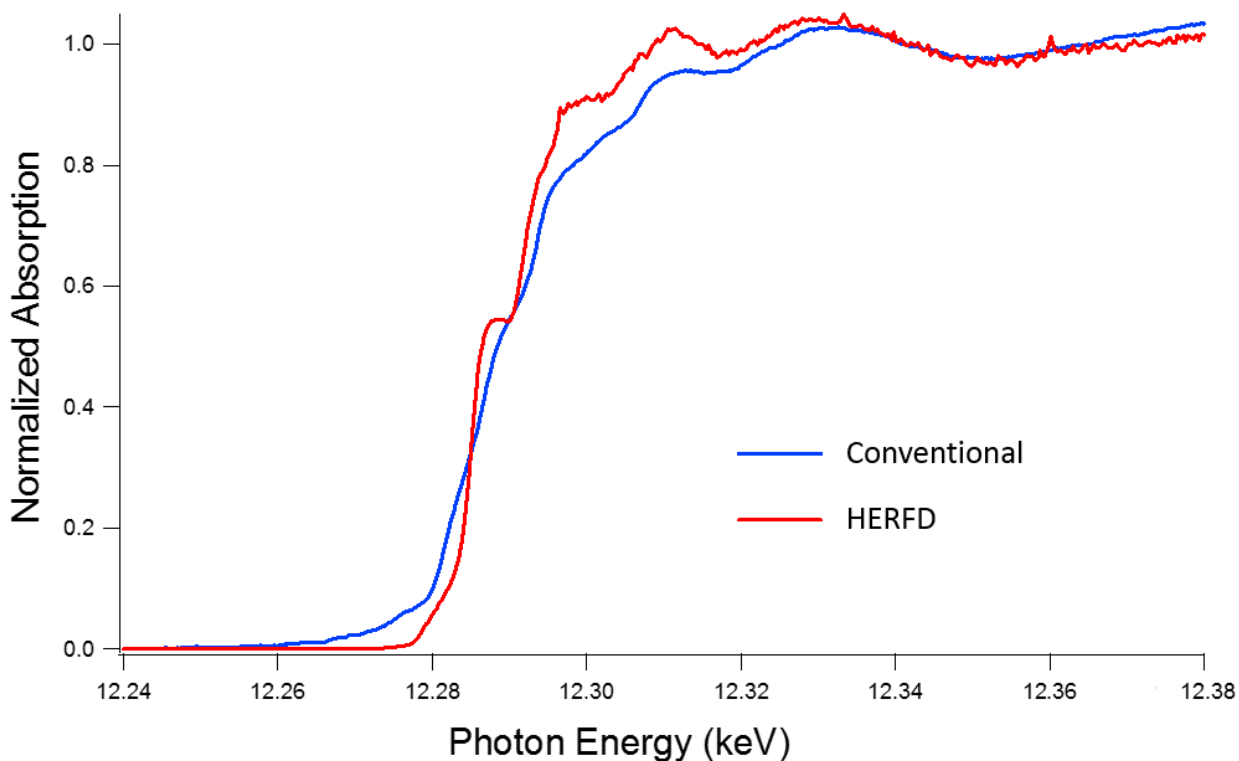


**Figure 4.10:** The spectra of cinnabar (HgS- $\alpha$ ) collected using a vertical Rowland circle geometry plotted to show contrast with the conventional HERFD result.

Clearly the spectral resolution attained using this system pales in comparison to that shown earlier using a horizontal Rowland circle, the major construction/functionality differences between the two systems leave this to be less than surprising. However, it should be noted that even with the somewhat lacking control systems for this orientation there is still a significant improvement in spectral resolution when compared to the conventional result. The pre-edge peak is apparent and clearly defined and the other peaks gained improved definition as well.

Moving forward with the vertical Rowland circle the major changes to construction required for optimal results would include switching to motorized z stages and adding a swivel stage (roll) to the detector allowing its face to be normal with the reflected fluorescence. At this time, it is hard to say if it is prudent to make these changes to the test system or if it is best wait till a more permanent system is being put into place to resume work with a vertical Rowland circle.

## **5 Further Developments and Conclusions**

In the following sections some potential testing and further developments as this project moves out of the feasibility study phase will be discussed. The goal of these continued measures would be to move towards a permanent HERFD endstation at HXMA that can complete novel research and provide a new form of experimentation at the Canadian Light Source. To achieve this further understanding of the focusing nature of the analyzed fluorescence is needed. In addition, the final HERFD arrangement must be able to produce spectra and maps at a speed that is practical for users (i.e. to complete a typical hard x-ray experimental run within a week). With these criteria met, the system would also strive to support a variety of sample environments to cater to a wider variety of experiments.

### **5.1 Area detection and ray tracing**

Within the HXMA system there is currently very little known about the beam profile of the analyzed photons after being focused by the crystal analyzer. While a general shape can be taken from literature based on the shape of a standard Johann system reflection (See [5]) the dimension and intensity profile specific to HXMA is unknown. To remedy this, a full ray tracing analysis through beam profile tracking could prove to be a fruitful investigation. The currently proposed way to accomplish this is to employ a pixel-hybrid detector (specifically a PILATUS3 100k [28]) allowing for constant beam shape monitoring. It is important to note that this type of detector isn't required for standard HERFD experimentation; however, it would be a major boon to this type of testing. The

pixel-hybrid's ability to show a continuous count profile will allow for imaging of the beam spot as the optical components are moved to optimize the signal as well as the difference in beam shape when there is a misalignment due to an optical component being positioned off the Rowland circle. Ideally, having a greater understanding of what is happening to the beam will allow for simpler and more streamlined adjustments to be made in active experiments. In addition, it would allow for a dynamic comparison between different analyzer crystals of the same cut ensuring the consistency and quality of said crystals.

As an aside, it is important to reiterate that this type of detector is not required for standard operation and something as simple as a photodiode can be used. This becomes more relevant when looking into working with a more sophisticated system that may wish to focus different crystals to varying Rowland circles and thus to different detectors.

## **5.2 Moving Vertical using a Multi-crystal analyzer system**

The next major development comes in two steps, the first of which would be realized practically immediately, while the latter will not come to full fruition until the dedicated HERFD system is complete. The first step is moving to a vertical Rowland circle orientation and has already been outlined in Section 4.4. Within this section it is mentioned that the current system lacks some of the required degrees of freedom in its motorized movement. The new stages required are motorized  $z$  stages for both the analyzer and detector as well as a swivel stage for the detector (which isn't inherently required to be motorized however it would be more ideal). Without the motorized  $z$  stages

(for both the detector and the analyzer) mapping is not possible and as such they are the current purchasing priority as the vertical Rowland circle is realized. The swivel stage is not as eminently necessary as the focused beam reaches the detector face on an angle of 6-15° off normal, so while not the ideal state for the detector to operate in it is still more than functional. To this point a manual swivel stage is all that is fully required as if the detector is tilted to be at the appropriate angle for the fluorescence line's maxima then angular deviations from normal on the detectors face when completing a map would be less than 2°.

Within the vertical Rowland circle system, the next step in moving towards a state-of-the-art arrangement would be the introduction of additional analyzers. The purpose of using a multi-crystal array comes in two parts, the first being the ability to cover a larger solid angle of the emitted fluorescence and the second is the need to only use Johann analyzer crystals of a limited size. The ability to cover more solid angle is simply to improve the analyzed signal strength allowing for faster data acquisition and stricter photon rection (i.e. a smaller detector aperture). The goal of this is reducing the time needed to produce high quality HERFD spectra and energy maps, which is paramount as the beamtime is a very limited quantity and users require a system that can be run efficiently and within strict time constraints. The reason for avoiding the use of larger crystals is to minimize the effects of Johann aberrations, the further one moves from the center of a Johann crystal the larger the deviation from the Rowland circle [5], [21]. This deviation is then cause for a larger range of photon energies to be reflected from the

analyzer crystal to the detector, in turn resulting in a decreased resolution which is counterproductive when actively seeking an energy resolution on the order of 1-2 eV.

### **5.3 Low Energy Extension**

The dedicated HERFD endstation at HXMA would seek to accommodate research with rare-earth elements and other samples with lower fluorescent energies. The HXMA beamline can produce a stable and scannable x-ray beam with energy as low as 5 keV. However, in its current state the HERFD system couldn't hope to run samples with emitted fluorescence in the lower end of the soft x-ray regime. The reason for this is the large scattering loss in the fluorescence x-ray pathway after the initial fluorescence. The distanced traveled in air would be just shy of a full meter and would result in the air absorbing upwards of 80% of the fluorescent photons at energies less than 7 keV.

This could be elevated by using a smaller Rowland circle however that would lead to a loss in resolution. The appropriate solution would be to contain all or a portion of the HERFD components in a glove bag/box and fill it with helium resulting in a signal intensity loss of less than 2% (for energies >4 keV) if all the optical components are enclosed. The complication that comes with the fully enclosed system is the time investment to displace the air and fill the chamber with helium every time a sample is to be changed. To address this either a motorized sample stand able to hold multiple samples could be used or the sample stand could be positioned outside of the enclosure. In the latter scenario the glove bag/box would have built in windows covered by a thin sheet of Kapton. This is a more practical system as HXMA users' complete experiments using a variety of sample

environments including cryostats and *in-situ* arrangements. The drawback of having the glove box/bag containing the detector and crystal analyzers is that when switching to a different energy range the analyzer crystals will likely have to be exchanged with a different cut to accommodate the new energy and as such the gas exchange in the chamber would still be required. With this in mind there would have to be considerations given to the time loss and if it is appropriate to contain the crystal analyzers in the enclosure or if it was more prudent to accept the signal loss and use a longer acquisition time with both the sample and crystal analyzers outside of the glove bag/box. Additionally, leaving these components outside of the glove bag/box would also increase accessibility to make manual adjustments.

The other major benefit of introducing a glove bag/box system is allowing for continually more dilute samples to be run due to a minimized signal loss. This would provide higher quality fluorescence results in addition to making naturally dilute samples (such as rare earth element geology samples) more viable.

## **5.4 Concluding Remarks**

In summary this feasibility study has proven to be a success with a very positive outlook. Considerable improvement in spectral resolution was observed in the cinnabar and metacinnabar samples with results approaching those produced by a dedicated endstation at ESRF. This provides promise that with tuning and improvements made to

the system competitive HERFD results could be produced by HXMA making the technique available for the first time in Canada.

When again possible, this study would continue its course by producing the energy maps as detailed in Section 4.3 and in doing so complete the course of its initial wave of testing. Through this the system's resolution could be accurately determined and a set of optimized HERFD scans could be taken to see the full capability of the single crystal system. Ideally this would be followed by a novel experiment to be completed using the HERFD system. This experiment would be very beamtime intensive but would be of indispensable merit to the continuation of the project and help move towards publishable results.

The work with HERFD at HXMA is far from over. There are many continual improvements that could be made to the prototype system. For instance, a crystal library will have to be collected to span the full range of scannable x-ray energies, routines to optimize mapping will have to be written and more efficient component alignment procedure must be put into place.

Beyond the prototype system a dedicated HERFD endstation within HXMA would be the pinnacle of this work. The construction of which would take the form of a multi-crystal analyzer array on a vertical Rowland circle contained within a glove bag/box. The currently constructed prototype system could remain functional while the dedicated endstation undergoes planning, this could help interested users begin working with a HERFD system prior to the endstation availability.

Ultimately, HERFD-XAS can be conducted a HXMA and if perused would provide a new avenue for quality science to be conducted at the CLS and in Canada as a whole. This feasibility has shown the promise and benefit of such a technique being perused.

## BIBLIOGRAPHY

- [1] K. Hämäläinen, D. P. Siddons, J. B. Hastings, and L. E. Berman, “Elimination of the inner-shell lifetime broadening in x-ray-absorption spectroscopy,” *Phys. Rev. Lett.*, vol. 67, no. 20, pp. 2850–2853, 1991, doi: 10.1103/PhysRevLett.67.2850.
- [2] O. Proux *et al.*, “High-Energy Resolution Fluorescence Detected X-Ray Absorption Spectroscopy: A Powerful New Structural Tool in Environmental Biogeochemistry Sciences,” *J. Environ. Qual.*, vol. 46, no. 6, pp. 1146–1157, 2017, doi: 10.2134/jeq2017.01.0023.
- [3] Z. Finfrock, “Private Communication.” 2019.
- [4] P. Glatzel *et al.*, “Reflections on hard x-ray photon-in/photon-out spectroscopy for electronic structure studies,” *J. Electron Spectros. Relat. Phenomena*, vol. 188, pp. 17–25, 2013, doi: 10.1016/j.elspec.2012.09.004.
- [5] D. B. Wittry and N. C. Barbi, “X-ray Crystal Spectrometers and Monochromators in Microanalysis,” *Microsc. Microanal.*, vol. 7, no. 2, pp. 124–141, 2001, doi: 10.1007/s100050010080.
- [6] M. Newville, “Fundamentals of XAFS,” *Rev. Mineral. Geochemistry*, vol. 78, pp. 33–74, 2014, doi: 10.2138/rmg.2014.78.2.
- [7] P. A. Lee, P. H. Citrin, P. Eisenberger, and B. M. Kincaid, “Extended x-ray absorption fine structure its strengths and limitations as a structural tool,” *Rev. Mod. Phys.*, vol. 53, no. 4, pp. 769–806, 1981, doi: 10.1103/RevModPhys.53.769.
- [8] J. Stohr, *NEXAFS Spectroscopy*. Springer-Verlag, 1996.
- [9] A. Bianconi, *X-ray Absorption: Principles, Applications, Techniques of EXAFS, SEXAFS and XANES*. Wiley, 1988.
- [10] Y. Joly, “X-ray absorption near-edge structure calculations beyond the muffin-tin approximation,” *Phys. Rev. B*, vol. 63, pp. 1–10, 2001, doi: 10.1103/PhysRevB.63.125120.
- [11] J. J. Rehr, J. J. Kas, F. D. Vila, M. P. Prange, and K. Jorissen, “Parameter-free calculations of X-ray spectra with FEFF9,” *Phys. Chem. Chem. Phys.*, vol. 12, no. 21, pp. 5503–5513, 2010, doi: 10.1039/b926434e.
- [12] P. Willmott, “An Introduction to Synchrotron Radiation: Techniques and Applications,” 1st ed., 2011, pp. 87–104.

- [13] H. Winick, *Synchrotron Radiation Sources — A Primer*. World Scientific, 1995.
- [14] F. M. F. De Groot, M. H. Krisch, and J. Vogel, “Spectral sharpening of the Pt L edges by high-resolution x-ray emission,” *Phys. Rev. B - Condens. Matter Mater. Phys.*, vol. 66, no. 19, pp. 1–7, 2002, doi: 10.1103/PhysRevB.66.195112.
- [15] M. Bauer, “HERFD-XAS and valence-to-core-XES: New tools to push the limits in research with hard X-rays?,” *Phys. Chem. Chem. Phys.*, vol. 16, no. 27, pp. 13827–13837, 2014, doi: 10.1039/c4cp00904e.
- [16] D. Sokaras *et al.*, “A seven-crystal Johann-type hard x-ray spectrometer at the Stanford Synchrotron Radiation Lightsource,” *Rev. Sci. Instrum.*, vol. 84, no. 5, pp. 1–8, 2013, doi: 10.1063/1.4803669.
- [17] S. Huotari, F. Albergamo, G. Vankó, R. Verbeni, and G. Monaco, “Resonant inelastic hard x-ray scattering with diced analyzer crystals and position-sensitive detectors,” *Rev. Sci. Instrum.*, vol. 77, no. 5, 2006, doi: 10.1063/1.2198805.
- [18] S. M. Butorin, K. O. Kvashnina, J. R. Vegelius, D. Meyer, and D. K. Shuh, “High-resolution X-ray absorption spectroscopy as a probe of crystal-field and covalency effects in actinide compounds,” vol. 113, no. 29, pp. 8093–8097, 2016, doi: 10.1073/pnas.1601741113.
- [19] U. Bergmann and Æ. P. Glatzel, “X-ray emission spectroscopy X-ray emission spectroscopy,” no. September, 2009, doi: 10.1007/s11120-009-9483-6.
- [20] Y. Maillard, J. Dousse, and J. Hozowska, “Energies and widths of atomic core-levels in liquid mercury,” *Eur. Physicsal J. D*, vol. 170, pp. 155–170, 2010, doi: 10.1140/epjd/e2010-00023-x.
- [21] J. Čermák, “Geometrical aberrations and physical characteristics of approximately focusing X-ray monochromators of Johann’s type,” *Czechoslov. J. Phys.*, vol. 17, no. 12, pp. 1073–1085, 1967, doi: 10.1007/BF01690825.
- [22] A. P. Shevelko, Y. S. Kasyanov, O. F. Yakushev, and L. V. Knight, “Compact focusing von Hamos spectrometer for quantitative x-ray spectroscopy,” *Rev. Sci. Instrum.*, vol. 73, no. 10, p. 3458, 2002, doi: 10.1063/1.1502013.
- [23] D. T. Jiang and E. Al., “Wiggler-based hard x-ray spectroscopy beamline at CLS.” pp. 800–803, 2007.
- [24] JJ X-ray, “About Slits,” 2020. <https://www.jjxray.dk/p/slits/>.
- [25] “XRStech,” 2019. <http://xrstech.com/>.
- [26] Thompson *et al.*, “X-ray Data Booklet,” *Lawrence Berkeley National Laboratory*. p.

176, 2009.

- [27] Hitachi, "Vortex-ME4 Xray Detector," *Catalog*, 2020. [https://www.hitachi-hightech.com/hhs-us/product\\_detail/?pn=ana-vortex-me4](https://www.hitachi-hightech.com/hhs-us/product_detail/?pn=ana-vortex-me4).
- [28] DECTRIS, "PILATUS3 S and X Series," 2016. <https://www.dectris.com/products/pilatus3/pilatus3-x-for-synchrotron/pilatus3-x-100k-a/>.
- [29] S. M. Heald, "Strategies and limitations for fluorescence detection of XAFS at high flux beamlines," *Synchrotron Radiat.*, pp. 436–445, 2015, doi: 10.1107/S1600577515001320.
- [30] M. Downs, R.T. , Hall-Wallace, "The American Mineralogist crystal structure database," *Am. Mineral.*, vol. 88, pp. 247–250, 2003.
- [31] B. E. Warren, *X-ray Diffraction*. New York: Dover Publications, 1990.
- [32] Huber, "Slit Systems," *Catalog*, 2020. .

## APPENDIX A: MOTION CONTROLS FOR THE HERFD SYSTEM

### Analyzer Stack

Motion	Manufacture	Part Number	Motor Type	Step Size (Full/Half Step)	Travel Range
X	Kohzu	XA16A-R202	5-phase Stepping Motor	4 $\mu m$ / 2 $\mu m$	$\pm 30$ mm
Y	AVS US Inc.	DS310-100	2-phase Stepping Motor	5 $\mu m$	$\pm 50$ mm
Z	Thorlabs	L490	Manual	N/A	57.3 mm
Pitch	Kohzu	RA07A-W02	5-phase Stepping Motor	0.004° / 0.002°	$\pm 135^\circ$
Roll	Kohzu	SA07A-RM02	5-phase Stepping Motor	0.0012° / 0.0006°	$\pm 10^\circ$

## Detector Stack

<b>Motion</b>	<b>Manufacture</b>	<b>Part Number</b>	<b>Motor Type</b>	<b>Step Size</b>	<b>Travel Range</b>
X	AVS US Inc.	DS310-100	2-phase Stepping Motor	5 $\mu$ m	$\pm$ 50 mm
Y	Huber	Surplus/Unknown	Manual	N/A	360°
Z	Thorlabs	L490	Manual	N/A	57.3 mm
Pitch	Huber	Surplus/Unknown	Manual	N/A	360°

## APPENDIX B: ENERGY RANGE OF VARIOUS SILICON CRYSTALS

Below is a table detailing the crystal cuts of silicon that result in a reflection for energies between  $\sim 2$  and  $10\text{ keV}$  when a Bragg condition with an angle greater than  $75^\circ$  is met. The associated energy range for each cut is listed as well as the harmonic reflections also in this energy range.

Crystal Cut {H, K, L}	Lattice Spacing ( $\text{\AA}$ )	Energy Range (eV)	Alternate Reflections	Additional Energy Ranges (keV)
{1,1,1}	3.1356	1977 - 2047	{3,3,3} {4,4,4} {5,5,5}	(5932 - 6140) (7909 - 8187) (9887 - 10234)
{2,2,0}	1.9201	3229 - 3342	{4,4,0}	(6458 - 6685)
{3,1,1}	1.6375	3786 - 3919		
{4,0,0}	1.3578	4566 - 4727	{8,0,0}	(9133 - 9454)
{5,3,1}	1.2460	4976 - 5151		
{4,2,2}	1.1086	5593 - 5789		
{5,1,1}	1.0452	5932 - 6140		
{5,3,1}	0.9180	6754 - 6991		
{4,4,2}	0.9052	6850 - 7090		

---

{6,2,0}	0.8587	7220 - 7474
{5,3,3}	0.8282	7486 - 7749
{6,2,2}	0.8188	7573 - 7839
{5,5,1}	0.7605	8153 - 8439
{7,1,1}	0.7605	8153 - 8439
{7,3,1}	0.7071	8769 - 9077
{5,5,3}	0.7071	8769 - 9077
{7,3,3}	0.6635	9345 - 9673
{8,2,2}	0.6400	9687 - 10027
{7,5,1}	0.6271	9887 - 10234
{8,4,0}	0.6072	10211 - 10570
{7,5,3}	0.5961	10401 - 10766